applied sciences

MDPI

Article

Numerical Investigation of Feedback Path Selection for Envelope Shaping in Fixed-Wing UAVs

Xiaolin Cao [1] and Xue Zhong [2,3,*]

[1] China Telecom Corporation Limited Heilongjiang Branch, Harbin 150001, China
[2] Department of Mechanics, Inner Mongolia University of Technology, Hohhot 010051, China
[3] Inner Mongolia Key Laboratory of Low-Altitude Technology and Engineering, Hohhot 010051, China
* Correspondence: xuezhong@imut.edu.cn

Featured Application

Architecture assessment for inversion based fixed-wing UAV control, supporting early decisions on whether an envelope feedback path should be retained before higher fidelity actuator, allocation, or hardware testing.

Abstract

Envelope feedback can improve a fixed-wing UAV state margin while increasing the command and input demand needed to realize it. We compare all eight combinations of speed force, angle-of-attack force and angle-of-attack moment at common gains in one inversion-based architecture. On 48 reused development cases, nested differences and independent directional Taylor propagation give the same outcome classifications. Angle-moment-only CAT and speed-force/angle-moment CVAT complete all cases with positive sampled margins, whereas angle-force configurations exhibit background-dependent input-request terminations. A frozen protocol for independent-input numerical evaluation then assesses four configurations on 100 new cases in two sampling ranges. CAT and CVAT complete all 50 cases in each range with positive sampled margins. CFULL completes 49/50 and 42/50. The stronger angle-margin target remains unmet. Common-state diagnostics trace force-path changes through command acceleration to elevator demand. A second-order attitude command tracker removes six terminations in a separate five-case comparison but increases position RMSE by 4.49–7.03 m on common complete pairs. Prescribed state-estimation errors substantially reduce completion. These results show task- and command-realization-dependent tradeoffs within the tested architecture. Conditional power accounting identifies retained coupling terms without establishing stability or invariance. The findings are limited by finite numerical resolution, qualified sampling, instantaneous actuation and the absence of atmospheric or hardware validation.

Keywords: fixed-wing unmanned aerial vehicle; flight control; trajectory tracking; envelope shaping; angle of attack; feedback path selection

Check for updates

Academic Editor: Yutaka Ishibashi

Received: 5 October 2026
Revised: 31 October 2026
Accepted: 2 November 2026
Published: 4 November 2026

Copyright: © 2026 by the authors. Licensee MDPI, Basel, Switzerland. This article is an open access article distributed under the terms and conditions of the Creative Commons Attribution (CC BY) license.

1. Introduction

Fixed-wing unmanned aerial vehicle (UAV) controllers often convert guidance objectives into virtual force or attitude commands and then into moments and control surface inputs. Guidance and path following methods organize desired motion [1,2], while constrained tracking methods address performance under vehicle limits [3]. This layered realization is central to the engineering problem studied here. During turning and deceleration, airspeed or angle of attack feedback may move the aircraft farther from a selected

boundary, but the same feedback also changes the attitude command used to realize the requested force. If that command is differentiated for rotational feedforward, the effect propagates to moment and surface demands. In controller development, an added protection path is therefore valuable only if its state level benefit is commensurate with the downstream demand that must be realized by the aircraft. Tracing this demand can inform subsequent actuator, allocation, hardware in the loop, and flight evaluation. Nonlinear inversion, command derivative generation, and constrained allocation all highlight different parts of this implementation chain [4–7].

Fixed-wing UAVs serve mapping and infrastructure-monitoring tasks that require coordinated motion along acquisition routes. For example, Bakuła et al. [8] used a fixed-wing multisensor platform for levee mapping, combining flight strips, trajectory processing and data calibration. This application motivates considering task execution and aircraft motion together. We examine whether a margin-improving feedback path imposes a downstream request that the chosen implementation can realize.

Relevant work addresses command modification and state constraints, aircraft envelope protection, energy-based feedback construction, and input realization. Constraint handling can enter this chain at several levels. Reference and command governors modify the commands supplied to a stabilized system [9], whereas barrier Lyapunov functions incorporate state constraints into the control storage [10]. Control barrier functions (CBFs) impose derivative conditions associated with forward invariance and can be combined with performance objectives in quadratic programs [11,12]. Higher order CBFs extend this approach to constraints for which inputs appear after further differentiation [13], with simultaneous state and input bounds requiring additional feasibility conditions [14].

In aircraft control, envelope protection has been studied using adaptive methods assessed in piloted simulation [15], phase plane limits with backstepping [16], and CBF quadratic programs [17]. Angle of attack constraints have been combined with saturation and fault tolerant tracking [18]. Control Lyapunov and barrier functions have also been applied to aircraft stability and safety [19], and flying wing envelope protection has been evaluated in piloted simulation [20]. Related work addresses autonomous aerobatic manoeuvres [21], attitude regulation near the envelope boundary [22], and nonlinear inversion at high angles of attack for low aspect ratio flying wing UAVs [23]. These studies motivate examining how the placement of envelope feedback affects the demands passed through a particular realization chain.

For the present comparison, energy methods provide a way to derive force and moment feedback from aerodynamic state gradients. Dissipativity relates storage change to supplied power [24]. Port-Hamiltonian modelling and interconnection and damping assignment use this relation in physical systems [25,26], and generalized canonical transformations provide a basis for trajectory tracking [27]. Fixed-wing Port-Hamiltonian control and passivity based cross track control incorporate aerodynamic state structure [28,29], while energy based methods also address position tracking for atmospheric vehicles [30]. We use the established recentering operation [31] to define storage gradients about moving nominal targets.

The resulting feedback still has to be realized by the aircraft. Nonlinear dynamic inversion provides one route from a virtual request to flight control inputs [4], with internal stability depending on the input and output organization [32]. Incremental inversion and adaptive variants address acceleration information, model dependence, and implementation delay [5,33]. Constrained control allocation distributes requests subject to effector bounds [6,7], and active set methods provide numerical solutions [34]. Restricting pseudo commands through an attainable moment set similarly accounts for lower layer author-

ity [35]. Nonlinear inversion has also been applied to fixed-wing trajectory tracking during ground taxiing, takeoff, and landing [36].

Protection placement has been examined by modifying the angle control organization of the Flying-V [37], intervening at the pseudo control level [38], and connecting collision avoidance and geofencing to lower level tracking [39]. Barrier filtering based on a closed loop model accounts for how an intervention changes closed loop behaviour [40]. Passivity preserving interventions [41] and port-transversal barriers [42] examine compatibility with system energy and interconnection structure. Within one fixed inversion based tracking architecture, we compare the margin benefit, tracking cost and realization demand of all eight combinations of speed force, angle force and angle moment at common final gains. This also tests whether a path behaves differently when the other paths are enabled.

Here a feedback path is a route by which the current state changes the requested aircraft input. The speed force acts along the velocity direction and modifies the translational force request. The angle of attack force acts through the translational angle gradient and also modifies that request. Both force paths pass through aerodynamic inversion to change the commanded attitude. The angle of attack moment instead enters the rotational moment request through the sensitivity of angle of attack to body rotation. All three ultimately share the same moment and surface realization. CVAT enables speed force and angle moment, CFULL enables all three paths, and CV enables speed force alone. CAT enables only angle moment, while C0 retains the base tracking controller with all envelope paths disabled. These five configurations are among the eight combinations obtained by independently enabling or disabling the three feedback paths.

The assessment separates reused development conditions from new independent inputs. The development evidence includes all eight configurations under two implementations of the same command derivative, common-state diagnostics and a finite neighbourhood of a difficult case. A second-order attitude command tracker tests a different command realization. Further studies examine numerical resolution and prescribed state-estimation errors. Finally, a frozen protocol evaluates four configurations on 100 newly generated cases in two sampling ranges, without retuning on their outcomes.

The contribution is a numerical architecture assessment that connects sampled state margins to tracking cost and downstream command, moment and input demand. Common-state evaluation distinguishes direct changes in the control map from subsequent trajectory divergence. Conditional power accounting identifies the coupling and discrepancy terms that remain when a feedback path is removed. Its sign-indefinite terms leave stability and invariance unproved. The findings describe task- and implementation-dependent tradeoffs and identify questions for subsequent actuator-aware and flight evaluation.

2. System Model and Problem Formulation

2.1. Physical Model and Reference

The numerical plant represents a rigid fixed-wing aircraft with six degrees of freedom and 13 integrated variables. Its aerodynamic polynomial structure and aircraft parameters are taken from the Generic Transport Model (GTM) entries in the generic nonlinear aerodynamic (GNA) model of Grauer and Morelli [43]. The project identifier T-2/GNA denotes this adopted computational benchmark. Supplementary Sections S1 and S2 give the coefficients, density law, and force axis convention.

Let $\mathcal{I}$ denote the north–east–down inertial frame and $\mathcal{B}$ the body frame, with body axes pointing forward, right, and down. The position $\boldsymbol{r} \in \mathbb{R}^3$ is expressed in $\mathcal{I}$ in metres. The body velocity is $\boldsymbol{v}^B = [u_B, v_B, w_B]^\top \in \mathbb{R}^3$ in metres per second. In inertial coordinates, $\boldsymbol{v} = \boldsymbol{R}\boldsymbol{v}^B$. The matrix $\boldsymbol{R} \in \mathrm{SO}(3)$ maps body components into inertial components, where $\mathrm{SO}(3) = \{\boldsymbol{R} : \boldsymbol{R}^\top \boldsymbol{R} = \boldsymbol{I}_3, \det \boldsymbol{R} = 1\}$ and $\boldsymbol{I}_3$ is the 3×3 identity matrix. A unit quaternion $\boldsymbol{q} =$

$[q_0, \boldsymbol{q}_v^\top]^\top \in \mathbb{R}^4$, with the scalar component first, represents the same rotation. The angular velocity $\boldsymbol{\omega} \in \mathbb{R}^3$ is expressed in $\mathcal{B}$ in radians per second. The integrated state is therefore $\boldsymbol{x} = [\boldsymbol{r}^\top, (\boldsymbol{v}^B)^\top, \boldsymbol{q}^\top, \boldsymbol{\omega}^\top]^\top \in \mathbb{R}^{13}$. Altitude is $h = -r_3$.

Subscripts 0 and a distinguish nominal controller parameters from actual plant parameters. The nominal controller mass and inertia are $m_0 > 0$ and $\boldsymbol{J}_0 > 0$. The actual plant values are $m_a > 0$ and the constant positive definite inertia matrix $\boldsymbol{J}_a \in \mathbb{R}^{3\times3}$ in kg m^2. With thrust T in newtons along the first body axis and surface deflections $\boldsymbol{\delta} = [\delta_a, \delta_e, \delta_r]^\top$ in radians, the plant obeys

$$\begin{aligned} \dot{\boldsymbol{r}} &= \boldsymbol{R}\boldsymbol{v}^B, & \dot{\boldsymbol{v}}^B &= -\boldsymbol{\omega} \times \boldsymbol{v}^B + g\boldsymbol{R}^\top \boldsymbol{e}_3 + (\boldsymbol{f}_a^B + T\boldsymbol{e}_1)/m_a, \\ \dot{q}_0 &= -\tfrac{1}{2}\boldsymbol{q}_v^\top \boldsymbol{\omega}, & \dot{\boldsymbol{q}}_v &= \tfrac{1}{2}(q_0 \boldsymbol{I}_3 + [\boldsymbol{q}_v]_\times)\boldsymbol{\omega}, \\ \boldsymbol{J}_a \dot{\boldsymbol{\omega}} &= \boldsymbol{\tau}_p - \boldsymbol{\omega} \times \boldsymbol{J}_a \boldsymbol{\omega}. \end{aligned} \tag{1}$$

Here $\boldsymbol{e}_1 = [1, 0, 0]^\top$ and $\boldsymbol{e}_3 = [0, 0, 1]^\top$ are coordinate basis vectors. The symbol g denotes gravitational acceleration, $\boldsymbol{f}_a^B$ is the aerodynamic force in body components, and $\boldsymbol{\tau}_p$ is the actual aerodynamic moment in body components, in newton metres. A dot denotes differentiation with respect to time t in seconds. The symbol $\top$ denotes transpose, and $[\boldsymbol{a}]_\times \boldsymbol{b} = \boldsymbol{a} \times \boldsymbol{b}$ defines the skew matrix of a three vector. Vector norms below are Euclidean. The unit quaternion constraint leaves 12 independent local physical coordinates.

Wind is zero, so air relative and ground relative velocities coincide. Actual airspeed V, angle of attack α, sideslip β, and dynamic pressure $\bar{q}$ are

$$V = \|\boldsymbol{v}^B\|, \qquad \alpha = \operatorname{atan2}(w_B, u_B), \qquad \beta = \arcsin(v_B/V), \qquad \bar{q} = \tfrac{1}{2}\rho(h)V^2, \tag{2}$$

where ρ is density in kg/m^3. Angles are computed in radians and converted by $180/\pi$ for figures and tables labelled in degrees. The implemented force and moment interface is

$$\boldsymbol{f}_a^B = \bar{q}S \begin{bmatrix} -C_D \cos\alpha + C_L \sin\alpha \\ C_Y \\ -C_D \sin\alpha - C_L \cos\alpha \end{bmatrix}, \qquad \boldsymbol{\tau}_p = \bar{q}S \begin{bmatrix} b_w C_l \\ \bar{c} C_m \\ b_w C_n \end{bmatrix}. \tag{3}$$

The wing area S, span b_w, and mean chord $\bar{c}$ have units m^2, m, and m. The six dimensionless coefficients $C_D, C_Y, C_L, C_l, C_m, C_n$ denote drag, side force, lift, roll moment, pitch moment, and yaw moment. They depend on aerodynamic states, angular rates, and deflections. Sideslip enters the polynomial model directly. Equation (3) is the force mapping used in the simulation and includes no additional sideslip rotation.

The desired position, velocity, and acceleration are the known functions $\boldsymbol{r}_d(t)$, $\boldsymbol{v}_d(t)$, and $\boldsymbol{a}_d(t)$ in $\mathcal{I}$, with units m, m/s, and m/s^2. The subscript d denotes a desired reference. Each vector is interpolated independently with a cubic spline. Consequently, $\boldsymbol{v}_d = \dot{\boldsymbol{r}}_d$ and $\boldsymbol{a}_d = \dot{\boldsymbol{v}}_d$ hold only approximately in the implementation. This distinction is retained in the power accounting. Table 1 gives the nominal aircraft parameters and controller settings. The rotational gains are fixed implementation settings rather than tuning results of this study.

Table 1. Nominal aircraft, controller, and numerical parameters. Actual plant parameters are perturbed only as specified in Section 4.1.

Quantity	Value	Unit
m_0	22.498181552	kg
$S,\ b_w,\ \bar{c}$	0.54831374208, 2.0875752, 0.278892	m^2, m, m

Table 1. *Cont.*

Quantity	Value	Unit
$J_{0,11}, J_{0,22}, J_{0,33}$	1.7991704174, 5.7676495522, 7.3946310902	kg m^2
$J_{0,13} = J_{0,31}$	−0.1626981538	kg m^2
g	9.80665	m/s^2
$\boldsymbol{K}_r$	$2.2498181552\boldsymbol{I}_3$	N/m
$\boldsymbol{D}_v$	$17.9985452416\boldsymbol{I}_3$	N s/m
k_R	80	N m
$\boldsymbol{K}_\omega$	$6\boldsymbol{I}_3$	N m s rad^{-1}
κ_V, κ_α	5, 0.001	J
h_L	0.0005	s
Relative/absolute tolerance	$2 \times 10^{-7}/10^{-9}$	solver settings
Maximum/saved output step	0.02/0.05	s

Aircraft values follow the GTM entries in Ref. [43], expressed in SI units. Unlisted inertia entries are zero. The gains $\boldsymbol{K}_r$ and $\boldsymbol{D}_v$ act on position and velocity errors, while k_R and $\boldsymbol{K}_\omega$ act on attitude and angular rate errors. Because angular rate is reported in rad/s, $\boldsymbol{K}_\omega$ has units of torque per angular rate, N m s rad^{-1}. The weights κ_V and κ_α multiply airspeed and angle of attack storage. The increment h_L is used in command differentiation and is distinct from the integration and output steps. Density follows Supplementary Section S2.

2.2. Tracking Objective and Design Boundaries

Define the position and inertial velocity errors as $\boldsymbol{e}_r = \boldsymbol{r} - \boldsymbol{r}_d$ and $\boldsymbol{e}_v = \boldsymbol{v} - \boldsymbol{v}_d$. The nominal inertial force request without shaping is

$$\boldsymbol{F}_0 = m_0(\boldsymbol{a}_d - g\boldsymbol{e}_3) - \boldsymbol{K}_r\boldsymbol{e}_r - \boldsymbol{D}_v\boldsymbol{e}_v, \tag{4}$$

where m_0 is the nominal mass, $\boldsymbol{K}_r \succ 0$ is a position gain in N/m, and $\boldsymbol{D}_v \succ 0$ is a velocity gain in N s/m. The notation $\succ 0$ denotes positive definiteness. Thrust, attitude, and aerodynamic moments jointly realize this virtual force request.

The design objective is to track the prescribed trajectory while shaping the approach to the actual state boundaries $V > V_{\min}$ and $\alpha < \alpha_{\max}$. These study boundaries describe the state response of interest, not a certified stall envelope. The realization has its own limits and preferences, listed in Table 2. In particular, the commanded angle α_c may exceed the preferred 10° while the actual angle remains below its design boundary. Finding a valid command in the inversion bracket $[0, 14°]$ is therefore a different question from maintaining the actual state margins. In Table 2, M_α is the minimum saved sample angle margin $\alpha_{\max} - \alpha$ over a completed run, using the sampling convention in Section 4.4.

Table 2. Distinct design boundaries, preferences, and model domain checks.

Object	Specified Value	Meaning
Actual speed V	$V > 31.176889725$ m/s	Lower study boundary
Actual angle α	$\alpha < 10°$	Upper study boundary
Moving centres	$V_t > V_{\min}$, $\alpha_t < \alpha_{\max}$	Nominal target feasibility
Command α_c	$\leq 10°$	Reporting preference
Inverse root	$0 \leq \alpha_c \leq 14°$	Search bracket
Thrust	$0 < T < 120$ N	Strict numerical guard
Aileron/elevator/rudder	$[-10, 10]/[-20, 10]/[-30, 30]°$	Inclusive model domain guards
Stronger angle margin	$M_\alpha \geq 0.25°$ in at least 90%	Original performance target
Speed recovery	$V - V_{\min} \geq 0.5$ m/s	Interior recovery target

The actual angle boundary is not an identified stall angle. A guard violation stops the run. No response after the limit is simulated.

The baseline uses the true plant state for feedback, zero wind, and no sensor noise or estimator dynamics. Within the permitted input domain, the plant applies the requested thrust T and surface deflections $\boldsymbol{\delta}$ instantaneously. Equality between controller requests and applied inputs is the instantaneous-actuation assumption of this baseline. An input-domain

guard checks the request after inversion and stops integration when it is inadmissible. The same checks apply to every configuration. No clamped surface response, actuator lag, or response after saturation is simulated. A separate sensitivity study replaces true-state feedback with prescribed estimates while retaining the omission of sensor and estimator dynamics (Section 4.2). The dynamic command tracker in Section 3.4 is upstream of the instantaneous input interface and is not a servo model.

Completion means reaching the specified final time without a terminating model or numerical check. A configuration with an angle path disabled can remain evaluable after crossing the actual angle study boundary, so completion alone does not imply positive state margins. Positive sampled margins additionally require a completed run with $M_V > 0$ and $M_\alpha > 0$. The stronger 0.25° margin target is a separate performance criterion, and the command preference and root-search bracket remain separate from both. None of these labels is used as a synonym for continuous safety. Section 4.4 specifies their counting rules.

Notation guide. Symbols retain the definitions in Sections 2 and 3. The configuration switches are listed in Table 3.

Symbol	Role and Units
$\boldsymbol{r}, \boldsymbol{v}^B, \boldsymbol{v}$	Inertial position (m), body and inertial velocity (m/s).
$\boldsymbol{R}, \boldsymbol{q}, \boldsymbol{\omega}$	Body-to-inertial rotation, unit quaternion, and body angular rate (rad/s).
$V, \alpha;\ V_t, \alpha_t$	Actual airspeed (m/s) and angle of attack (rad). Moving nominal centres.
$\boldsymbol{r}_d, \boldsymbol{v}_d, \boldsymbol{a}_d$	Desired inertial position, velocity, and acceleration (m, m/s, m/s^2).
$\boldsymbol{e}_r, \boldsymbol{e}_v, \boldsymbol{e}_R, \boldsymbol{e}_\Omega$	Position, velocity, attitude, and angular-rate errors.
$\boldsymbol{F}_c, \boldsymbol{\tau}_c;\ T, \boldsymbol{\delta}$	Virtual force (N) and moment (N m). Thrust (N) and surface requests (rad).
$\alpha_c, \boldsymbol{C}_c, \widehat{\boldsymbol{\omega}}_c, \hat{\boldsymbol{a}}_c$	Command angle, attitude, and nominal-predictor rate and acceleration (rad, dimensionless, rad/s, rad/s^2).
$\mathcal{B}_V, \mathcal{B}_\alpha, W$	Dimensionless recentered storages and analytical total storage (J).
s_V, s_{AF}, s_{AT}	Binary switches for speed force, angle force, and angle moment.
M_V, M_α, E_r, D_F	Sampled speed/angle margins (m/s, rad), position RMSE (m), and peak physical force residual (N).
$\boldsymbol{Z}_{\text{est}}, \boldsymbol{e}_\theta$	Prescribed state estimate and right attitude-error rotation vector (rad), Section 4.2.
$\boldsymbol{C}_a, \boldsymbol{C}_f, \boldsymbol{\omega}_f, \boldsymbol{a}_f$	Algebraic/filtered attitudes and filter rate/acceleration (rad/s, rad/s^2), Section 3.4.
CF16, H-I, H-X	16 rad/s command tracker. Original-range and expanded-range independent inputs.
Δ, CI	Within-case on-minus-off or explicitly named paired difference. Confidence interval.

Table 3. All eight internal path combinations at the common final gains. C0 retains the base tracking controller. C_{011} is registered in this revision. Geometry, plant, inversion-root and input-request domains apply to every configuration.

Configuration	s_V	s_{AF}	s_{AT}	Enabled Barriers
C0	0	0	0	none
CV	1	0	0	speed
CAF	0	1	0	angle
CAT	0	0	1	angle
CVAF	1	1	0	speed + angle
CVAT	1	0	1	speed + angle
C_{011}	0	1	1	angle
CFULL	1	1	1	speed + angle

3. Selective Envelope Shaping Architecture

3.1. Recentered Storage and State Geometry

We construct the shaping terms from storage gradients that vanish at the nominal targets. Recentring supplies this property by subtracting the value and tangent of a convex primitive at a selected centre [31], within the broader barrier Lyapunov function approach to constrained control [10]. For a scalar state ξ, an interior centre ξ_t, and a twice differentiable primitive ϕ, define

$$\mathcal{B}_\phi(\xi, \xi_t) = \phi(\xi) - \phi(\xi_t) - \phi'(\xi_t)(\xi - \xi_t), \qquad b_\phi = \phi'(\xi) - \phi'(\xi_t). \tag{5}$$

Primes denote scalar derivatives. The subscript t denotes a moving target centre and not a derivative. The two dimensionless primitives are

$$\phi_V(V) = -\log \frac{V - V_{\min}}{\sigma_V}, \quad V > V_{\min}, \qquad \phi_\alpha(\alpha) = -\log \frac{\alpha_{\max} - \alpha}{\sigma_\alpha}, \quad \alpha < \alpha_{\max}, \tag{6}$$

where $\sigma_V > 0$ and $\sigma_\alpha > 0$ have units m/s and rad, respectively, and make the logarithms dimensionless. Their values cancel in the recentered expressions. Write $\mathcal{B}_V, \mathcal{B}_\alpha$ and b_V, b_α for Equation (5) applied to these primitives. Explicitly,

$$b_V = -\frac{1}{V - V_{\min}} + \frac{1}{V_t - V_{\min}}, \qquad b_\alpha = \frac{1}{\alpha_{\max} - \alpha} - \frac{1}{\alpha_{\max} - \alpha_t}. \tag{7}$$

Both storage terms and their state gradients vanish at their centres, and the storage terms diverge at their respective boundaries.

The centre $V_t = \|\boldsymbol{v}_d\|$ uses the desired speed. The centre α_t is obtained by nominal force inversion for the feedforward request $m_0(\boldsymbol{a}_d - g\boldsymbol{e}_3)$ at the desired velocity and reference altitude. It expresses the nominal trajectory's force requirement, distinct from the trim angle of a perturbed plant. Reference generation checks that both centres are strictly inside their domains before accepting a scenario.

Airspeed changes through translation, whereas angle of attack also changes through body rotation. To express these two contributions, define the inertial unit velocity direction $\boldsymbol{t}_I = \boldsymbol{v}/V$, the body and inertial angle gradients $\boldsymbol{g}_B, \boldsymbol{g}_I$ in s/m, and the dimensionless body rotation sensitivity $\boldsymbol{h}_B$ by

$$\boldsymbol{g}_B = \frac{[-w_B, 0, u_B]^\top}{u_B^2 + w_B^2}, \qquad \boldsymbol{g}_I = \boldsymbol{R}\boldsymbol{g}_B, \qquad \boldsymbol{h}_B = \boldsymbol{g}_B \times \boldsymbol{v}^B. \tag{8}$$

On the regular domain $V > 0$ and $u_B^2 + w_B^2 > 0$,

$$\dot{V} = \boldsymbol{t}_I^\top \dot{\boldsymbol{v}}, \qquad \dot{\alpha} = \boldsymbol{g}_I^\top \dot{\boldsymbol{v}} + \boldsymbol{h}_B^\top \boldsymbol{\omega}. \tag{9}$$

Thus the angle gradient has both translational and rotational actions. In coordinated motion, $\boldsymbol{h}_B$ points along the positive second body axis under the adopted convention. The connection between aerodynamic states and energy based fixed-wing control is established in prior work [28,29].

3.2. Three Selectable Feedback Paths

Let κ_V and κ_α be nonnegative storage weights in joules. Define the following gradient vectors with velocity units

$$\boldsymbol{q}_V = \frac{\kappa_V}{m_0} b_V \boldsymbol{t}_I, \qquad \boldsymbol{\theta} = \frac{\kappa_\alpha}{m_0} b_\alpha \boldsymbol{g}_I, \tag{10}$$

both in m/s. The three selectable terms are

$$\boldsymbol{F}_V = -\boldsymbol{D}_v \boldsymbol{q}_V, \qquad \boldsymbol{F}_\alpha = -\boldsymbol{D}_v \boldsymbol{\theta}, \qquad \boldsymbol{\tau}_\alpha = -\kappa_\alpha b_\alpha \boldsymbol{h}_B. \tag{11}$$

They are called V force, angle of attack (AoA) force, and AoA torque, respectively. The first two are inertial force requests in newtons, whereas the third is a body moment request in newton metres. These terms enter the force and moment requests through the shared aircraft realization.

For binary switches $s_V, s_{AF}, s_{AT} \in \{0, 1\}$, the commanded inertial force and added body moment are

$$\boldsymbol{F}_c = \boldsymbol{F}_0 + s_V \boldsymbol{F}_V + s_{AF} \boldsymbol{F}_\alpha, \qquad \boldsymbol{\tau}_{\text{env}} = s_{AT} \boldsymbol{\tau}_\alpha. \tag{12}$$

The subscripts AF and AT identify the angle force and angle torque paths, and "env" denotes the envelope shaping moment. A disabled path is omitted before its barrier is evaluated, so switching it off also removes the corresponding logarithm evaluation.

For the isotropic $\boldsymbol{D}_v$ used here, $\boldsymbol{t}_I^\top \boldsymbol{g}_I = 0$ makes the two force terms orthogonal. This instantaneous geometry need not hold for arbitrary gain matrices and does not separate their effects on the shared attitude and moment realization. Figure 1 shows that shared route. All eight switch combinations test the three paths and their interactions through this same realization route.

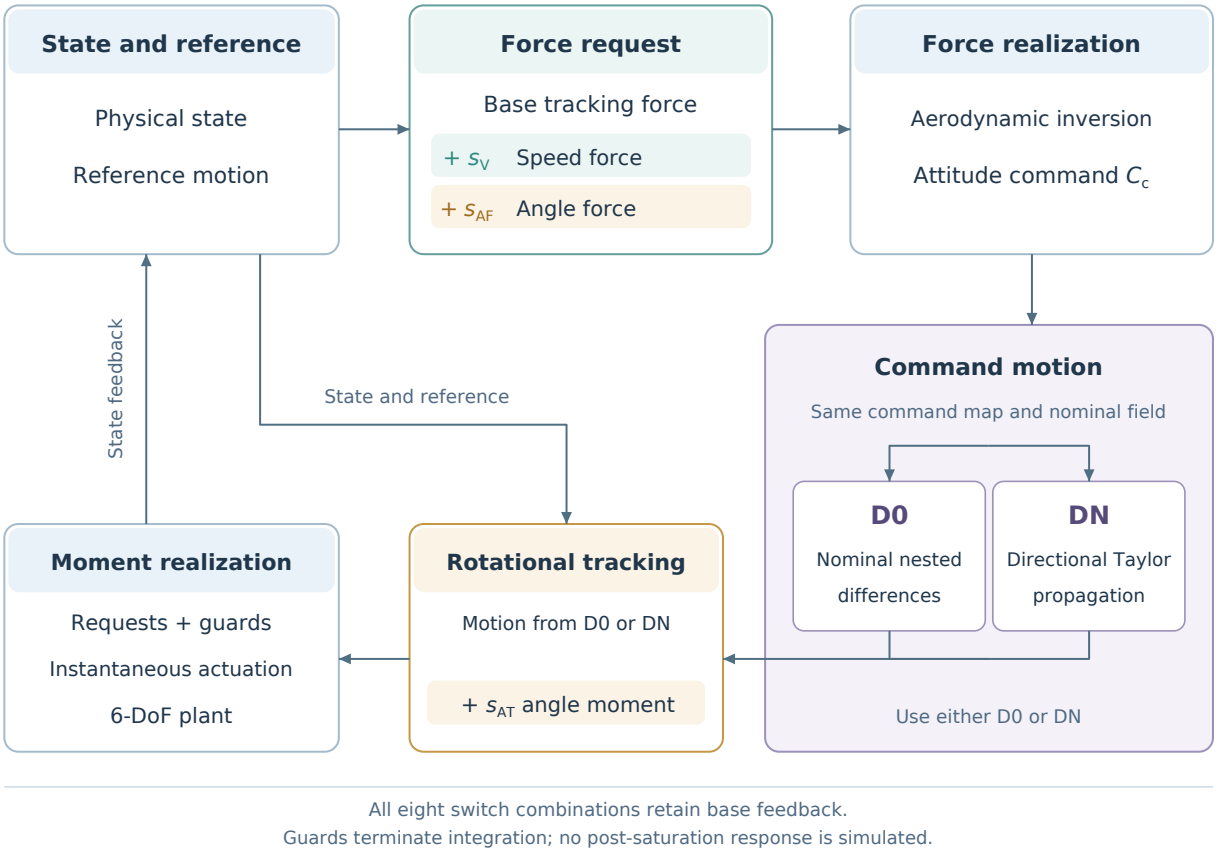


Figure 1. Three independently switched envelope paths in the common tracking architecture. Force paths change the force and attitude command, while the angle-moment path enters the rotational request. D0 uses nominal nested differences. DN independently differentiates the same nominal field and command map by directional Taylor propagation. Either derivative branch supplies command motion to rotational tracking. The dynamic alternative in Equation (22) replaces this command triplet in a separate comparison. All eight switch combinations retain the base controller. Input guards terminate the numerical model. Instantaneous actuation is assumed and infeasible requests are not redistributed.

3.3. Aerodynamic and Rotational Realization

To realize $\boldsymbol{F}_c$, we resolve it along the air path and solve a coupled lift–thrust inversion within the dynamic inversion framework [4,32]. Define the actual climb angle

$\gamma = \operatorname{atan2}(-v_3, \sqrt{v_1^2 + v_2^2})$ and course $\chi = \operatorname{atan2}(v_2, v_1)$, where v_i is inertial velocity component i. The orthonormal air path directions are $\boldsymbol{t}_I$, $\boldsymbol{n}_\gamma = [-\sin\gamma\cos\chi, -\sin\gamma\sin\chi, -\cos\gamma]^\top$, and $\boldsymbol{n}_\chi = [-\sin\chi, \cos\chi, 0]^\top$. Then

$$X = \boldsymbol{t}_I^\top \boldsymbol{F}_c, \quad Y_\gamma = \boldsymbol{n}_\gamma^\top \boldsymbol{F}_c, \quad Y_\chi = \boldsymbol{n}_\chi^\top \boldsymbol{F}_c, \quad N = \sqrt{Y_\gamma^2 + Y_\chi^2}, \quad \mu_c = \operatorname{atan2}(Y_\chi, Y_\gamma). \tag{13}$$

Here X is the tangential force, N is the magnitude of the normal force, and μ_c is the commanded bank angle. The quantities Y_γ and Y_χ are components of the normal force. All four force scalars have units N. The nominal lift and drag at zero angular rate and zero surface deflection are $L_0(V, \alpha, h)$ and $D_0(V, \alpha, h)$. The root for α_c and the thrust request projected through the actual angles are

$$N = L_0(V, \alpha_c, h) + [D_0(V, \alpha_c, h) + X]\tan\alpha_c, \qquad T = \frac{D_0(V, \alpha_c, h) + X}{\cos\alpha\cos\beta}. \tag{14}$$

The denominator uses the actual angles. A positive projection, nonzero N, and a bracketed root are required. A safeguarded Newton and bisection procedure searches $[0, 14°]$. Supplementary Section S3 gives its derivative and stopping rules. The requested attitude that maps body coordinates into inertial coordinates is

$$\boldsymbol{C}_c = \boldsymbol{R}_z(\chi)\boldsymbol{R}_y(\gamma)\boldsymbol{R}_x(\mu_c)\boldsymbol{R}_y(\alpha_c), \tag{15}$$

where $\boldsymbol{R}_x, \boldsymbol{R}_y, \boldsymbol{R}_z$ are right handed elementary rotations about their indicated axes. All factors and $\boldsymbol{C}_c$ are dimensionless 3×3 matrices. The force feedback determines this attitude command. Switching a force path therefore changes the map to be differentiated.

Command motion is obtained by differentiating the feedback attitude along a local nominal prediction field. Geometric control with moving references provides the rotational feedforward structure [44], while command derivative generation and filtering are established implementation issues in nonlinear control [45–47]. Let $C(t, \boldsymbol{Z})$ denote the current mapping from state and time to command attitude, with $\boldsymbol{Z} = (\boldsymbol{r}, \boldsymbol{v}, \boldsymbol{R}, \boldsymbol{\omega})$. A local nominal prediction $\Phi_\epsilon(\boldsymbol{Z}; t)$ over signed time increment ϵ uses $\boldsymbol{a}_N = g\boldsymbol{e}_3 + \boldsymbol{F}_c/m_0$ and is defined by

$$\boldsymbol{r}^+ = \boldsymbol{r} + \epsilon\boldsymbol{v} + \tfrac{1}{2}\epsilon^2\boldsymbol{a}_N, \quad \boldsymbol{v}^+ = \boldsymbol{v} + \epsilon\boldsymbol{a}_N, \quad \boldsymbol{R}^+ = \boldsymbol{R}\exp([\boldsymbol{\omega}]_\times\epsilon), \quad \boldsymbol{\omega}^+ = \boldsymbol{\omega}. \tag{16}$$

The superscript + denotes a prediction for either sign of ϵ, not the next accepted physical state. Here exp is the matrix exponential. The predictor holds angular velocity fixed and uses nominal translational acceleration, omitting actual angular acceleration and plant parameter errors.

With $h_L = 0.0005$ s, the implemented command rate $\widehat{\boldsymbol{\omega}}_c$ and acceleration $\hat{\boldsymbol{a}}_c$ are obtained from the following nested centred differences.

$$\begin{aligned} \boldsymbol{D}_C &= \frac{C(t + h_L, \Phi_{h_L}) - C(t - h_L, \Phi_{-h_L})}{2h_L}, \\ \widehat{\boldsymbol{\omega}}_c(t, \boldsymbol{Z}) &= \operatorname{vee}\Big(\operatorname{skew}(\boldsymbol{C}_c^\top \boldsymbol{D}_C)\Big), \\ \hat{\boldsymbol{a}}_c(t, \boldsymbol{Z}) &= \frac{\widehat{\boldsymbol{\omega}}_c(t + h_L, \Phi_{h_L}) - \widehat{\boldsymbol{\omega}}_c(t - h_L, \Phi_{-h_L})}{2h_L}. \end{aligned} \tag{17}$$

Arguments $(\boldsymbol{Z}; t)$ of Φ are suppressed in Equation (17). Each nested rate evaluation constructs its own nominal neighbours and queries the known reference at those times. For an arbitrary 3×3 matrix $\boldsymbol{M}$, $\operatorname{skew}(\boldsymbol{M}) = (\boldsymbol{M} - \boldsymbol{M}^\top)/2$ extracts the skew part, and vee inverts $[\cdot]_\times$. The computed rate and acceleration, marked by hats, are expressed in command frame coordinates, in rad/s and rad/s^2. They approximate command motion along the nominal predictor and require no future state measurements. Even as h_L decreases, this construction retains the predictor's frozen angular velocity and nominal

acceleration. It therefore does not become differentiation along the actual perturbed physical trajectory merely by refining the increment. The difference is retained explicitly in the command-motion terms of Section 3.6. The original ensemble and historical runs use this D0 implementation. The DN implementation below is evaluated alongside D0 in the new complete comparison. It does not replace the historical D0 records.

We denote the original nested finite-increment implementation by D0 and add DN, a second-order directional Taylor implementation of its zero-increment target. DN differentiates the same algebraic command map and nominal field. It does not use the actual perturbed plant vector field. Let

$$\begin{aligned} \boldsymbol{f}_N &= (\boldsymbol{v}, \boldsymbol{a}_N, \boldsymbol{R}[\boldsymbol{\omega}]_\times, \boldsymbol{0}), \quad L_N = \partial_t + D_{\boldsymbol{Z}}[\,\cdot\,]\boldsymbol{f}_N, \\ \boldsymbol{\omega}_c^N &= \mathrm{vee}\big(\mathrm{skew}(\boldsymbol{C}_c^\top L_N \boldsymbol{C}_c)\big), \quad \boldsymbol{a}_c^N = L_N \boldsymbol{\omega}_c^N. \end{aligned} \tag{18}$$

Each inner evaluation in Equation (17) reconstructs the nominal field at its own state. Accordingly, DN includes the second directional term $L_N \boldsymbol{F}_c / m_0$ in the velocity jet. Differentiating a single curve with acceleration frozen at the starting point would omit this term. The implicit aerodynamic roots are evaluated by the original bracketed solver and differentiated by the implicit-function equations on regular branches. The separately stored reference splines retain their own piecewise derivatives. The reference, gains, force request and algebraic attitude are retained. DN supplies $\boldsymbol{\omega}_c^N, \boldsymbol{a}_c^N$ consistently in the rate error, transport, and acceleration terms of Equation (20). Supplementary Section S3 gives the propagation equations and rejection conditions. DN adds no dynamic state and is not a command filter.

For the geometric rotational errors, let $\boldsymbol{A}_c = \boldsymbol{R}^\top \boldsymbol{C}_c$ map command frame components into body components, and let $\boldsymbol{Q}_c = \boldsymbol{C}_c^\top \boldsymbol{R}$. Define

$$\boldsymbol{e}_R = \tfrac{1}{2}\,\mathrm{vee}(\boldsymbol{Q}_c - \boldsymbol{Q}_c^\top), \quad \boldsymbol{e}_\Omega = \boldsymbol{\omega} - \boldsymbol{A}_c \widehat{\boldsymbol{\omega}}_c, \quad \Psi = \tfrac{1}{2}\,\mathrm{tr}(\boldsymbol{I}_3 - \boldsymbol{Q}_c). \tag{19}$$

The trace operator is tr. The attitude error vector $\boldsymbol{e}_R$ and scalar Ψ are dimensionless, while $\boldsymbol{e}_\Omega$ is a body angular rate error. Geometric attitude errors and feedforward terms for moving references are well established [44]. The nominal total aerodynamic moment requested here is

$$\boldsymbol{\tau}_c = \boldsymbol{\omega} \times \boldsymbol{J}_0 \boldsymbol{\omega} - k_R \boldsymbol{e}_R - \boldsymbol{K}_\omega \boldsymbol{e}_\Omega - \boldsymbol{J}_0 [\boldsymbol{\omega}]_\times \boldsymbol{A}_c \widehat{\boldsymbol{\omega}}_c + \boldsymbol{J}_0 \boldsymbol{A}_c \hat{\boldsymbol{a}}_c + \boldsymbol{\tau}_{\mathrm{env}}, \tag{20}$$

where $k_R > 0$ is the attitude gain in N m and $\boldsymbol{K}_\omega \succ 0$ is the angular rate gain in N m s rad^{-1} when angular rate is expressed in rad/s. Denote the acceleration feedforward component by $\boldsymbol{\tau}_{\mathrm{acc}} = \boldsymbol{J}_0 \boldsymbol{A}_c \hat{\boldsymbol{a}}_c$. For D0, Equation (20) uses the numerical command motion from Equation (17). The DN implementation substitutes Equation (18) consistently. Both add $\boldsymbol{\tau}_{\mathrm{env}}$ to the moment request. The full nominal aerodynamic moment is inverted, so a separate aerodynamic damping term is not added.

At a fixed state, the nominal moment is affine in the surface deflections and is written as $\boldsymbol{\tau}_0 + \boldsymbol{B}_\delta \boldsymbol{\delta}$, where $\boldsymbol{\tau}_0$ is the moment at zero surface deflection in N m and $\boldsymbol{B}_\delta \in \mathbb{R}^{3\times 3}$ has units N m/rad. The implementation solves

$$\boldsymbol{\delta} = \boldsymbol{B}_\delta^{-1} (\boldsymbol{\tau}_c - \boldsymbol{\tau}_0) \tag{21}$$

with a linear system solver, checks its conditioning, and applies the input guards. This nonredundant 3 × 3 map has a unique exact solution at a fixed state when nonsingular. If that solution exceeds a bound, a bounded allocator could trade moment error against admissibility, but cannot be assumed to realize the same moment exactly by redistribution. Constrained least-squares allocation provides such a residual-based design route [6,7,48]. It is not implemented here.

3.4. Dynamic Attitude Command Tracker

To test dependence on command realization, let $\boldsymbol{C}_a = \mathbb{C}(t, \boldsymbol{Z})$ be the algebraic attitude in Equation (15) and introduce

$$\begin{aligned} \boldsymbol{Q}_f &= \boldsymbol{C}_a^{\top}\boldsymbol{C}_f, \qquad \boldsymbol{e}_f = \tfrac{1}{2}\,\mathrm{vee}(\boldsymbol{Q}_f - \boldsymbol{Q}_f^{\top}), \\ \dot{\boldsymbol{C}}_f &= \boldsymbol{C}_f[\boldsymbol{\omega}_f]_{\times}, \qquad \boldsymbol{a}_f = \dot{\boldsymbol{\omega}}_f = -\omega_n^2\boldsymbol{e}_f - 2\zeta\omega_n\boldsymbol{\omega}_f. \end{aligned} \tag{22}$$

The initialization is $\boldsymbol{C}_f(0) = \boldsymbol{C}_a(0, \boldsymbol{Z}_0)$ and $\boldsymbol{\omega}_f(0) = 0$. The primary setting CF16 uses $\omega_n = 16$ rad/s and $\zeta = 1$. A unit quaternion and three rates add seven stored coordinates to the 13-coordinate plant. The quaternion constraints reduce the number of independent degrees of freedom. Equations (19) and (20) consistently substitute $(\boldsymbol{C}_f, \boldsymbol{\omega}_f, \boldsymbol{a}_f)$ for the command triplet. Force inversion and thrust still use the original algebraic request, so attitude lag can change force realization.

This tracker adopts the dynamic command-generation idea discussed in command filtering [45–47]. It includes no rate clipping, actuator dynamics or compensation state and is not a complete command-filtered backstepping or dynamic-surface controller. Their closed-loop guarantees therefore do not transfer to this augmented aircraft. DN differentiates the original nominal command field. CF16 changes the dynamics generating the command. They are not successive numerical refinements of one method. Supplementary Section S17 gives the augmented interface and its limited theoretical scope.

3.5. Internal Controller Configurations

The full comparison crosses the three independent switches in Table 3. The previously unnamed combination $(0, 1, 1)$ is denoted C_{011} here. It combines angle force and angle moment without speed force. All configurations retain the original base tracking, attitude and rate feedback. Each enabled path uses its unchanged final weight, and the common angle storage is counted once even when both angle paths are active.

The speed barrier is evaluated only when $s_V = 1$, and the shared angle barrier only when $s_{AF} = 1$ or $s_{AT} = 1$. Disabled barriers are skipped before evaluating their logarithms or derivatives. Physical geometry, plant, inversion-root and input-request domains still apply. Disabling angle shaping leaves the physical stopping rules unchanged. A completed C0 or CV trajectory can therefore have an observed negative angle margin. Such an outcome remains in the common state-level assessment. At a common valid state, switching only s_{AT} leaves force, attitude command and its supplied motion unchanged. The direct total-moment difference equals the angle-moment term. Closed-loop trajectories need not coincide.

In the complete development comparison, every configuration is evaluated under D0 and DN. C0 is the internal unshaped baseline, not an external established controller. The seven-mode study at $\kappa_\alpha = 0.01$ J remains a historical development record in Supplementary Section S8. The new complete comparison uses $\kappa_V = 5$ J and $\kappa_\alpha = 0.001$ J without tuning individual configurations.

3.6. Conditional Power Accounting and Local Analysis

The conditional accounting identity below tracks the coupling, effective inputs, command motion and reference inconsistency that remain after a path is removed. It holds on regular intervals inside the stated domains. The retained sign-indefinite powers leave closed-loop stability, dissipativity and positive invariance unproved, and do not determine configuration performance. Removing AoA force changes the control request, but the same angle storage still contributes to the analysis. We use storage and supply rates [24–26] to follow the remaining coupling, realization, and command motion terms, including the

supply terms relevant to passivity and barrier interventions [41]. For CVAT and CFULL, the analytical storage in joules contains one AoA storage term,

$$W = \tfrac{1}{2}\boldsymbol{e}_r^\top \boldsymbol{K}_r \boldsymbol{e}_r + \tfrac{1}{2} m_0 \boldsymbol{e}_v^\top \boldsymbol{e}_v + k_R \Psi + \tfrac{1}{2}\boldsymbol{e}_\Omega^\top \boldsymbol{J}_0 \boldsymbol{e}_\Omega + \kappa_V \mathcal{B}_V + \kappa_\alpha \mathcal{B}_\alpha. \tag{23}$$

The storage measures tracking errors and boundary approach for control analysis, not battery or fuel consumption. We differentiate it on intervals with differentiable trajectories and command maps, interior actual states and centres, regular aerodynamic geometry, and constant plant parameters in Equation (1). Persistence of these conditions is assumed rather than established by the identity.

Let $\boldsymbol{F}_p = \boldsymbol{R}(\boldsymbol{f}_a^B + T\boldsymbol{e}_1)$ be the actual inertial force excluding gravity. The reported physical force residual is $\boldsymbol{d}_F^{\text{phys}} = \boldsymbol{F}_p - \boldsymbol{F}_c$. For error dynamics written with nominal mass, the effective force and moment inputs are

$$\begin{aligned} \boldsymbol{d}_F^{\text{eff}} &= (m_0/m_a)\boldsymbol{F}_p - \boldsymbol{F}_c, \\ \boldsymbol{d}_\tau^{\text{eff}} &= \boldsymbol{J}_0 \boldsymbol{J}_a^{-1}(\boldsymbol{\tau}_p - \boldsymbol{\omega}\times \boldsymbol{J}_a\boldsymbol{\omega}) - (\boldsymbol{\tau}_c - \boldsymbol{\omega}\times \boldsymbol{J}_0\boldsymbol{\omega}). \end{aligned} \tag{24}$$

Their units are N and N m, respectively. The mass and inertia factors account for writing the actual dynamics with nominal controller parameters. Under parameter mismatch, each effective input differs from its corresponding physical residual. The nominal algebraic moment residual of Equation (21) is a separate quantity.

A second difference arises because the feedback attitude is evaluated along the physical trajectory, while its supplied rate and acceleration come from the nominal predictor. The resulting rate discrepancy enters the configuration kinematics, and the derivative discrepancy enters the angular momentum dynamics. Together with the reference interpolation discrepancies, these quantities are

$$\begin{aligned} \boldsymbol{\rho}_r &= \boldsymbol{v}_d - \dot{\boldsymbol{r}}_d, & \boldsymbol{\rho}_v &= \boldsymbol{a}_d - \dot{\boldsymbol{v}}_d, \\ \boldsymbol{\Omega}_c &= \operatorname{vee}(\boldsymbol{C}_c^\top \dot{\boldsymbol{C}}_c), & \boldsymbol{\nu} &= \boldsymbol{\Omega}_c - \widehat{\boldsymbol{\omega}}_c, \\ \boldsymbol{d}_c &= \hat{\boldsymbol{a}}_c - \frac{d\widehat{\boldsymbol{\omega}}_c}{dt} - \boldsymbol{\Omega}_c \times \widehat{\boldsymbol{\omega}}_c. \end{aligned} \tag{25}$$

$\boldsymbol{\rho}_r$ and $\boldsymbol{\rho}_v$ are inertial reference discrepancies in m/s and m/s^2. The command rate along the actual trajectory, $\boldsymbol{\Omega}_c$, and the discrepancies $\boldsymbol{\nu}$ and $\boldsymbol{d}_c$ are expressed in the command frame. All derivatives in Equation (25) are along the physical trajectory. They are analytical quantities and need not be directly available to the controller.

Let $\bar{\boldsymbol{e}}_v = \boldsymbol{e}_v + \boldsymbol{q}_V$. For CVAT, differentiation of Equation (23) gives the exact accounting identity, under the stated domain conditions,

$$\dot{W} = -\bar{\boldsymbol{e}}_v^\top \boldsymbol{D}_v \bar{\boldsymbol{e}}_v - \boldsymbol{e}_\Omega^\top \boldsymbol{K}_\omega \boldsymbol{e}_\Omega + \Pi_V + \Pi_{\alpha 0} + \mathcal{P}_{\text{ext}}, \tag{26}$$

where the nominal coupling powers in watts are

$$\begin{aligned} \Pi_V &= m_0 \boldsymbol{q}_V^\top \boldsymbol{a}_d - \boldsymbol{q}_V^\top \boldsymbol{K}_r \boldsymbol{e}_r - \kappa_V \phi_V''(V_t)(V - V_t)\dot{V}_t, \\ \Pi_{\alpha 0} &= m_0 \boldsymbol{\theta}^\top \boldsymbol{a}_d - \boldsymbol{\theta}^\top \boldsymbol{K}_r \boldsymbol{e}_r - \boldsymbol{\theta}^\top \boldsymbol{D}_v \bar{\boldsymbol{e}}_v + \kappa_\alpha b_\alpha \boldsymbol{h}_B^\top \boldsymbol{A}_c \widehat{\boldsymbol{\omega}}_c \\ &\quad - \kappa_\alpha \phi_\alpha''(\alpha_t)(\alpha - \alpha_t)\dot{\alpha}_t, \end{aligned} \tag{27}$$

and the physical, command motion, and reference power terms are

$$\begin{aligned} \mathcal{P}_{\text{ext}} = (\bar{\boldsymbol{e}}_v + \boldsymbol{\theta})^\top \boldsymbol{d}_F^{\text{eff}} + \boldsymbol{e}_\Omega^\top \boldsymbol{d}_\tau^{\text{eff}} + \boldsymbol{e}_\Omega^\top \boldsymbol{J}_0 \boldsymbol{A}_c \boldsymbol{d}_c - k_R \boldsymbol{e}_R^\top \boldsymbol{A}_c \boldsymbol{\nu} \\ + \boldsymbol{e}_r^\top \boldsymbol{K}_r \boldsymbol{\rho}_r + m_0 \boldsymbol{e}_v^\top \boldsymbol{\rho}_v. \end{aligned} \tag{28}$$

In CVAT, $\boldsymbol{F}_\alpha$ is disabled but $\boldsymbol{\theta}$ remains in the storage derivative away from the centre. Its contribution appears in $\Pi_{\alpha 0}$ and in the effective input powers. The omission therefore

involves nominal coupling, moving centre power, and mass effects as well as the physical force residual, rather than just $\boldsymbol{\theta}^{\top}\boldsymbol{d}_F^{\mathrm{phys}}$. Supplementary Section S5 derives the corresponding balances for both configurations. Since switching the path also changes the command coordinates, a comparison of their full power balances depends on the states and commands at which they are evaluated.

This diagnostic evaluates a separately defined ideal model. Its matrix differs from the implemented physical closed-loop Jacobian, so it supplies neither a physical stability certificate nor a configuration ranking. For this calculation, let $\boldsymbol{z} = [\boldsymbol{e}_r^{\top}, \boldsymbol{e}_v^{\top}, \boldsymbol{\eta}_R^{\top}, \boldsymbol{e}_\Omega^{\top}]^{\top} \in \mathbb{R}^{12}$, where $\boldsymbol{\eta}_R$ is an infinitesimal attitude error coordinate in radians. A manually defined ideal model $\dot{\boldsymbol{z}} = \mathbf{A}(t)\boldsymbol{z}$ and symmetric quadratic storage matrix $\mathbf{P}(t)$ give

$$\mathbf{Q}(t) = -\big(\dot{\mathbf{P}} + \mathbf{P}\mathbf{A} + \mathbf{A}^{\top}\mathbf{P}\big). \tag{29}$$

The matrices are 12×12, and $\mathbf{P}$ is one half of the Hessian of the specified ideal quadratic storage. The full definition, matrix blocks, existing finite-grid results, and their limitations are retained in Supplementary Section S6. Connecting this ideal construction to the physical closed loop would require continuous bounds and a justified coordinate mapping. The conditional power identity does not supply that connection.

4. Numerical Study Design

4.1. Shared Model and Development Evidence

All studies use MATLAB R2018a, the plant in Section 2.1, and the common final gains in Table 1, including $\kappa_V = 5$ J and $\kappa_\alpha = 0.001$ J. Controllers retain nominal parameters while each perturbed plant has constant case-specific mass, inertia and aerodynamic coefficients. Configurations share the physical initial state, reference and plant within a case. No separately optimized gains are used to rank configurations.

The retained nominal manoeuvre starts at 38.1 m/s and altitude 365.76 m, turns toward radius 159.1015625 m during 5–13 s, and decelerates to 31.8 m/s during 18–28 s. Independently interpolated position, velocity and acceleration splines use a 0.005 s reference grid with 0.5 s endpoint extensions. Figure 2 shows this reference. Interpolation discrepancies are quantified in Supplementary Section S3.

The 48 accepted challenge cases E48 vary the task, initial state and plant using MATLAB `twister` seed 3495 (Supplementary Section S11). They were reused for development, weight selection and diagnosis and remain a development set. Initial states use perturbed-plant trim plus offsets, so initialization assumes knowledge of that plant. The earlier seven-configuration comparison and weight scan used a different angle weight and remain historical records in Sections S8 and S9. The original three-configuration ensemble and its 47 common complete pairs are retained in Sections S10 and S18.

The final-gain comparison crosses eight configurations with D0 and DN on E48, giving 768 logical runs. The archived nominal task N00 supplies 16 separately reported runs. Inputs and decision rules were fixed before integration. No input was resampled, retrimmed or removed after a termination. Baseline integration uses `ode45`, relative/absolute tolerances $2 \times 10^{-7}/10^{-9}$, maximum step 0.02 s, horizon 45 s and output spacing 0.05 s. D0 uses $h_L = 0.0005$ s, independently of the solver step and output grid. Twelve switch edges use on-minus-off differences and six interaction faces require all four matched trajectories to complete. Supplementary Section S16 records the full matrix and selective refinements.

Common-state evaluation holds the physical state, reference and gains fixed while changing the controller map. It separates direct path effects from trajectory divergence. A prespecified nine-coordinate design around Scenario 26 contains 55 unique conditions comprising 19 center/axis points, a 5×5 radius–speed slice and 16 signed joint points, with shared nodes counted once. CV, CVAT and CFULL are evaluated under D0 and DN.

Detailed ranges, event diagnostics and subsequent six-point noncenter refinements are in Sections S14–S16. These finite local conditions are not independent random evaluation samples or a certified continuous neighbourhood.

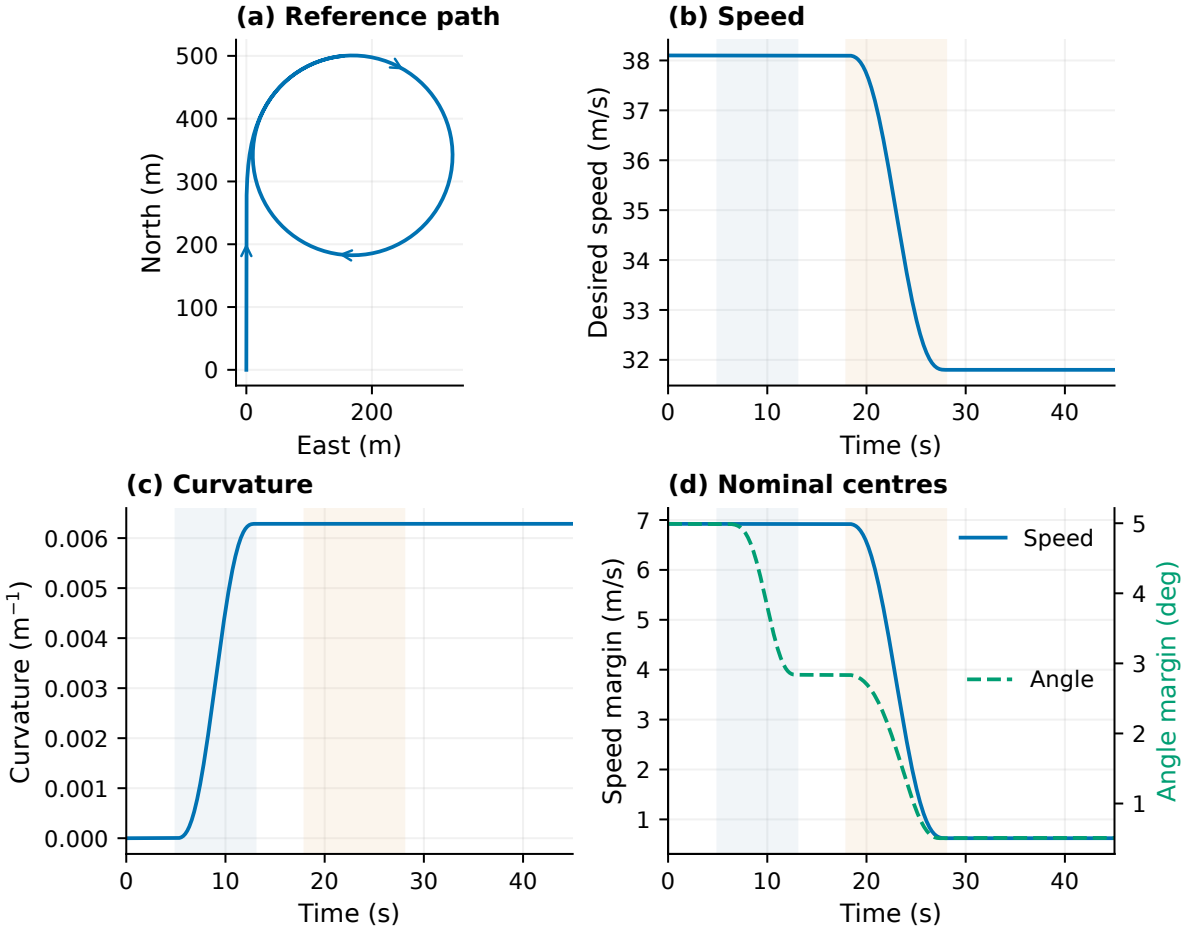


Figure 2. Nominal reference for the turning and decelerating numerical study. Panel (**a**) shows the horizontal reference path, with arrows indicating the direction of travel. Panel (**b**) shows desired speed, panel (**c**) prescribed curvature, and panel (**d**) nominal target margins for speed and angle of attack (AoA). In panels (**b–d**), pale blue-gray shading marks the curvature transition from 5 to 13 s, and pale orange shading marks the deceleration from 18 to 28 s. All panels describe the nominal reference and moving centres, before the tracking response or the 48 perturbed scenarios are considered.

4.2. Command Realization, Numerical Resolution and Estimation Errors

The filter comparison reuses S01, S26, S07, S08 and S45 with all eight configurations under DN and CF16. Main tolerances are $2 \times 10^{-8}/10^{-10}$, maximum step and evaluation spacing 0.005 s. S01/S26 are also refined to $2 \times 10^{-9}/10^{-11}$ with 0.0025 s maximum step and spacing. Bandwidth sensitivities at 8 and 32 rad/s cover S01/S26 only (Section S17).

A separate 70-run numerical study compares CVAT/CFULL at eight development cases, varying tolerances, maximum step and D0 increment separately. The common evaluation grid is 0.005 s, with the historical 0.05 s subset retained. The design and case-specific limits are in Section S18. Neither these checks nor DN provide a rigorous global error bound.

For estimation sensitivity, the controller receives $\boldsymbol{Z}_{\mathrm{est}}$ while the plant and evaluation use the true state. Position, body velocity and body rate estimates add prescribed errors, while $\boldsymbol{R}_{\mathrm{est}} = \boldsymbol{R}\exp([\boldsymbol{\epsilon}_\theta]_\times)$. Twelve independent stationary first-order autoregressive channels are generated at 0.01 s with correlation time 0.2 s and linearly interpolated. Low-level

stationary standard deviations are 0.2 m, 0.05 m/s, 0.05° and 0.05°/s for the four groups. High-level values are four times larger on the same standardized streams. Five reused cases and four configurations (CV, CAT, CVAT, CFULL) give 20 zero-error runs and 60 runs at each nonzero level, with three paired streams per case. Integration uses $2 \times 10^{-8}/10^{-10}$ tolerances, 0.005 s maximum step and evaluation spacing, and D0 with $h_L = 0.0005$ s. This prescribed-error study does not model an estimator, sensor hardware, wind or turbulence (Section S19).

4.3. Independent Inputs and Prespecified Statistics

A protocol fixed configurations, gains, sampling, numerical settings and endpoints before generating 100 new cases, with 50 in the original sampling ranges (H-I) and 50 with all range half-widths enlarged by 1.5 about unchanged centers (H-X). Each case uses CV, CAT, CVAT and CFULL, giving 400 integrations but 100 independent case inputs. The two layers are analyzed separately. Input seeds are 27,192,601 and 27,192,602 using MATLAB `twister`. Nominal reference qualification precedes outcomes. All rejected candidates are logged. Inputs are checked for exact duplication against development and previously accepted inputs, then sealed before integration. No tuning follows the independent-input evaluation outcomes.

The independent study retains D0 and the baseline solver settings but evaluates at 0.005 s (9001 samples for a complete run). The reference qualification grid remains 0.05 s. The two primary binary endpoints are completion and completion with both sampled margins positive. Each uses all 50 cases per layer. Four exact two-sided paired McNemar tests compare CFULL with CVAT (two endpoints in each layer), with one Holm family at $\alpha = 0.05$. Case-level bootstrap intervals accompany paired proportion differences. Individual proportions use 95% Wilson intervals. Continuous differences require joint completion and use 10,000 case-level resamples for paired-median percentile intervals. Seeds, ranges, qualification rules and complete outcome accounting are in Section S20. These conditional distributions and finite samples do not establish a population success rate of one.

4.4. Performance Measures and Paired Comparisons

Each comparison changes the feedback paths in Equation (12) while holding plant parameters, reference, initial state, gains, and numerical settings fixed within the case. We first examine whether each configuration completes the manoeuvre. All configurations are paired with C0, and all twelve switch edges and six faces retain their common complete horizons and explicit sample counts. The historical CVAT/CFULL pair is also retained for continuity.

For saved times t_k, $k = 1, \ldots, n_s$, where n_s is the number of samples in a completed trajectory, define

$$\begin{aligned} M_V &= \min_k (V(t_k) - V_{\min}), \quad & M_\alpha &= \min_k (\alpha_{\max} - \alpha(t_k)), \\ E_r &= \left(\frac{1}{n_s} \sum_{k=1}^{n_s} \|\boldsymbol{e}_r(t_k)\|^2 \right)^{1/2}, \quad & D_F &= \max_k \|\boldsymbol{d}_F^{\text{phys}}(t_k)\|. \end{aligned} \tag{30}$$

The quantities M_V, M_α, E_r, D_F have units m/s, rad, m, and N. E_r is the position root mean square error (RMSE) on the saved sample grid. D_F is a force realization discrepancy and is not an energy or actuator work metric. Positive sampled margins require $M_V > 0$ and $M_\alpha > 0$ for a completed run. They do not bound extrema between saved samples.

The development ensemble counts use denominator 48. Each independent layer uses 50 so that an incomplete run remains part of the comparison. An incomplete run cannot establish the full-horizon margin or command criteria. Its unavailable full-horizon

values remain missing. It stays in the denominator, but an unobserved full-horizon criterion is not relabelled as an observed state-boundary violation. The stronger criterion is $M_\alpha \geq 0.25°$, originally targeted in at least 90% of cases. The separate command preference is $\max_k \alpha_c(t_k) \leq 10°$.

For the cases completed by both CVAT and CFULL, differences and ratios are computed within each matched case before aggregation. Ratios use CVAT divided by CFULL. Medians and the 95th percentile use sorted finite values and linear interpolation at rank $1 + (n-1)p/100$, where n is the selected case count and p is the percentile level. The resulting historical summaries are descriptive statistics conditional on joint completion. Supplementary Section S18 adds post hoc paired-median bootstrap intervals without treating these reused cases as an independent-input evaluation set. The 47-case subset does not replace the all-case completion and threshold counts. A partial failed trajectory is used only for time-local diagnostics. Its partial-horizon cost is not substituted for an unavailable full-horizon cost. Supplementary Section S12 gives the exact failure and threshold conventions.

For the speed isolation comparison of C0 and CV, both runs begin with a positive speed margin. The useful question is how quickly that margin recovers further into the interior. With recovery target $\Delta_V = 0.5$ m/s and final time $T_f = 20$ s, we measure the accumulated shortfall as

$$\mathcal{E}_V = \int_0^{T_f} \max\{0, \Delta_V - [V(t) - V_{\min}]\}\, dt, \tag{31}$$

evaluated by the trapezoidal rule on saved samples spaced by 0.02 s. Its unit is metres. Recovery time is the earliest saved time at which the margin reaches Δ_V and remains above $\Delta_V - 10^{-9}$ m/s at every later saved sample. Exposure and recovery therefore measure approach to an interior speed margin. They do not measure recovery after crossing $V_{\min}$.

5. Results

5.1. Complete Configuration Comparison

Of the 768 recorded E48 runs, 756 completed 45 s and 12 terminated at the elevator-request lower guard. D0 and DN agree on the completion and threshold classifications (Table 4). CAF/CVAF terminate at S07, and all four AF-containing modes terminate at S26. C0 and CV complete S26 with a negative sampled angle margin. Completion therefore does not itself establish protection. CAT and CVAT complete all 48 cases with positive sampled margins, but meet the stronger 0.25° angle criterion in only 38 and 37 cases. The best count, 38/48 (79.2%), remains below the original 90% target. All 16 separate N00 runs complete. They do not enlarge the E48 denominator.

The twelve single-path contrasts in Figure 3 show background-dependent effects. Under DN, adding angle moment to C0 increases the minimum angle margin in 44/48 common complete cases (median 0.00725°), while increasing position RMSE in all 48 (median 0.06499 m). On CAT→CVAT, speed force increases speed margin in 25 cases and decreases it in 23. Corresponding angle-margin counts are 22 and 26. RMSE increases in 47 cases and decreases in S16, with median change +0.00922 m. For this turning design, CAT uses fewer enabled paths and has lower RMSE in 47 matched cases, while the speed- and angle-margin differences have mixed directions.

The four AF-on edges have 46, 46, 47 and 47 common complete cases. Their DN RMSE changes are negative throughout, with medians between -8.63×10^{-5} and -1.29×10^{-4} m. These small recorded reductions coexist with request terminations and remain subject to the numerical qualifications below. The C_{011} result shows that AF-associated difficulty can occur without speed force. At S07, enabling AT on either AF-containing background changes termination to completion. At S26 it does not. This closed-loop dependence is distinct from the fact that AT does not directly change the force-command map at a fixed

state. The six four-cell interaction faces and their missing-data patterns are retained in Section S16.

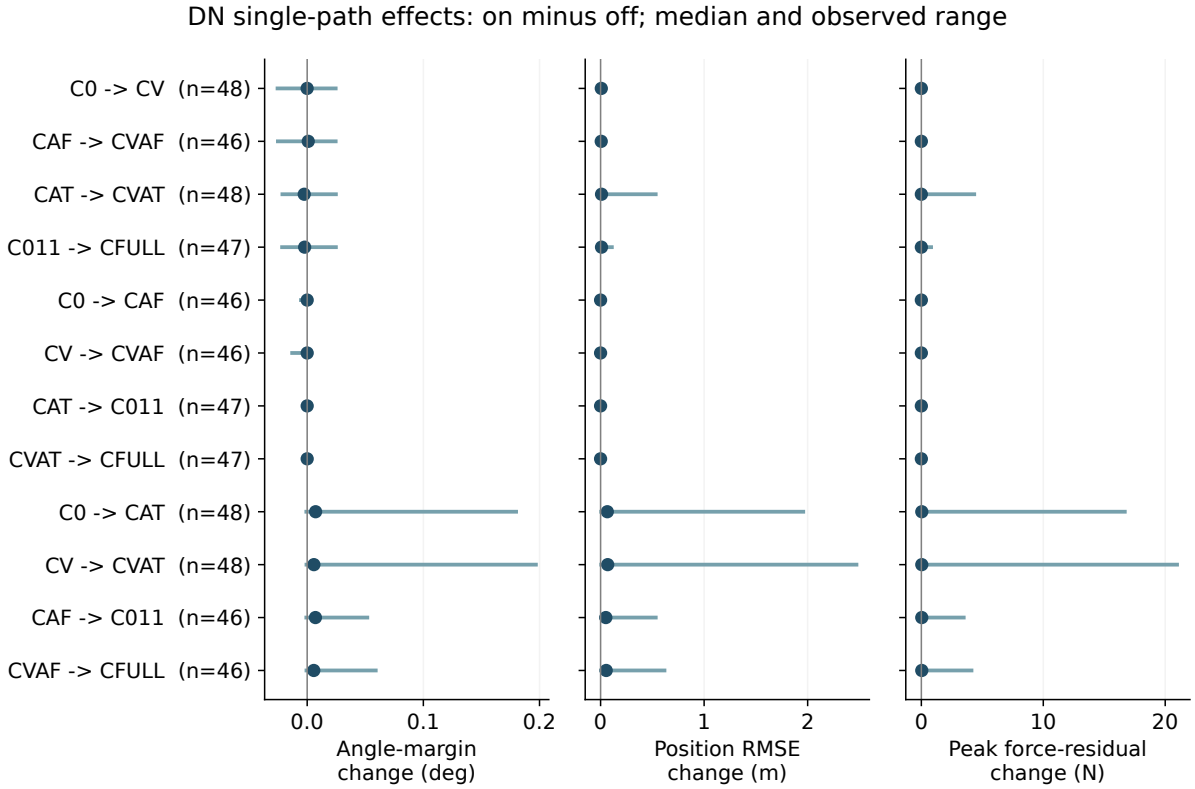


Figure 3. Twelve DN single-path contrasts, on minus off, evaluated within each common complete case. Markers show medians and horizontal segments the observed paired ranges. N is the actual common metric count. D0 results, all C0 contrasts, six four-cell faces and binary patterns are retained in Supplementary Section S16 and the computational tables.

Table 4. Complete final-gain E48 comparison. Every entry has planned denominator 48. C = completion. V^+ and α^+ count positive sampled speed and angle margins separately. A = angle margin at least 0.25°. Q = command angle at most 10°. S = scientific termination. U = technical undetermined. N = available full-horizon metric records. Criteria count established full-horizon outcomes. Missing values are not zeros or observed violations. All completed runs have positive speed margin, so the joint positive-margin count equals the angle-positive count here.

Mode	Impl.	C	V^+	α^+	A	Q	S	U	n
C0	D0	48	48	47	37	47	0	0	48
C0	DN	48	48	47	37	47	0	0	48
CV	D0	48	48	47	37	47	0	0	48
CV	DN	48	48	47	37	47	0	0	48
CAF	D0	46	46	46	37	46	2	0	46
CAF	DN	46	46	46	37	46	2	0	46
CAT	D0	48	48	48	38	45	0	0	48
CAT	DN	48	48	48	38	45	0	0	48
CVAF	D0	46	46	46	37	46	2	0	46
CVAF	DN	46	46	46	37	46	2	0	46
CVAT	D0	48	48	48	37	44	0	0	48
CVAT	DN	48	48	48	37	44	0	0	48
C011	D0	47	47	47	38	45	1	0	47
C011	DN	47	47	47	38	45	1	0	47
CFULL	D0	47	47	47	37	44	1	0	47
CFULL	DN	47	47	47	37	44	1	0	47

5.2. Numerical Qualification of Small Paired Effects

The historical D0 CVAT/CFULL comparison has 47 common complete cases, excluding S26 while retaining its termination in the all-case counts. New post hoc bootstrap summaries use signed CFULL-minus-CVAT differences (Section S18). Median angle-margin change is -4.06×10^{-6} degrees, with 95% interval $[-2.71\times10^{-5}, -1.01\times10^{-6}]$. Median position-RMSE change is -1.29×10^{-4} m, with interval $[-4.86\times10^{-4}, -2.26\times10^{-5}]$. These are descriptions of reused cases conditional on completion, not physical equivalence or precision guarantees.

The separate 70-run numerical study records 66 completions and four S26/CFULL request terminations. Completion and threshold classifications are unchanged across the inspected settings, but the sign of the CFULL-minus-CVAT angle-margin difference changes at S01, S02 and S40. Only seven of the historical 47 pairs are individually covered by this study. The other 40 lack this individual numerical check. An interval excluding zero does not resolve a numerical or engineering significance threshold. The earlier eight-configuration refinements at S01/S26/S08/S45 likewise retain classifications (56 completions, eight terminations), without establishing a global error budget. Small effects and interaction signs remain qualified in Section S16.

5.3. Scenario 26 and Its Local Neighbourhood

In the retained three-configuration S26 record, CV completes with angle margin $-0.1620°$, whereas CVAT has $+0.03490°$ at increased RMSE (4.179 to 6.650 m) and peak physical force residual (11.09 to 32.06 N). CFULL terminates near 28.35 s, so its full-horizon costs are unavailable. Figure 4 includes a separately integrated partial event history. It is not a saturated actuator response. The original ordinary last saved time, invalid solver trial and localized event state are different records (Section S14).

At the retained common event state, switching CVAT to CFULL adds only about 0.301 N of angle force while changing command pitch acceleration from approximately -0.014 to 9.365 rad/s^2 under D0. DN reduces the CFULL value to 9.206 rad/s^2 and moves its elevator request from approximately $-20.000°$ to $-19.669°$. Thus the numerical implementation affects the boundary request but does not explain the entire path difference. Integrations from the original initial state still terminate under both D0 and DN. Their ordinary invalid trial times, 28.345654 and 28.347313 s, are not event roots.

All 55 local conditions retain CVAT completion and CFULL request termination under both derivative implementations. CV has a negative sampled angle margin throughout. CVAT has positive margins but meets neither the 0.25° angle target nor the 10° command preference at any point. Its D0 angle margins range from 0.02463° to 0.05468°. The subsequent six-point noncenter refinements retain classifications, leaving the other 48 noncenter points without individual fine checks. No sampled classification transition is found, and no continuous region is inferred. At 24 inspected common states, DN gives positive CFULL-minus-CVAT command pitch-acceleration and acceleration-moment changes with a more negative elevator request. This supports the mechanism at those states. It does not individually verify every local trajectory. Sections S14–S16 retain the signed component and conditioning diagnostics.

5.4. Changing the Command Realization

Across five reused cases and eight configurations, DN completes 34/40 runs with 32 positive-margin completions. CF16 completes all 40 with positive sampled margins (Table 5). The four S26 and two S07 DN request terminations therefore disappear under this command realization. On all 34 common complete pairs, however, CF16 increases position RMSE by 4.49–7.03 m and physical force-residual RMS by 13.33–22.57 N. Angle margins increase by 0.197–0.437°, while peak absolute elevator request decreases by 0.210–0.469°.

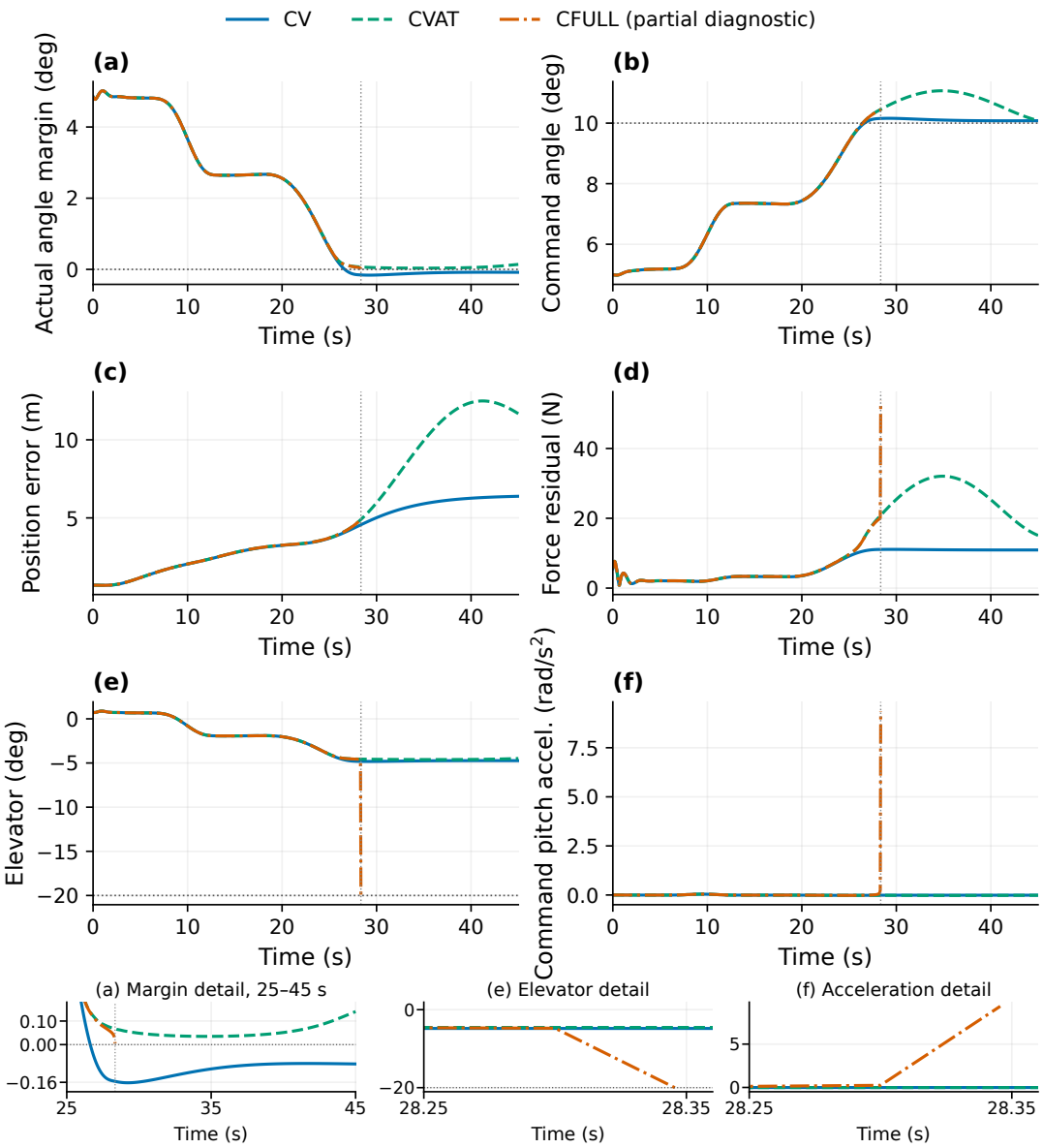


Figure 4. Scenario 26 at final weights $\kappa_V = 5$ J and $\kappa_\alpha = 0.001$ J. Panel (**a**) shows actual angle of attack margin, with a local view of 25–45 s near the zero boundary. Panel (**b**) shows command angle and its 10° preference. Panels (**c**,**d**) show position error norm and physical force residual norm. Panel (**e**) shows elevator command and its −20° lower guard. Panel (**f**) shows numerically generated command pitch acceleration. CV and CVAT cover 0–45 s. CFULL is the separately computed partial event diagnostic history and ends near 28.35 s. The solid blue, dashed green and dash-dotted orange curves show CV, CVAT and the partial CFULL diagnostic, respectively. The vertical dotted lines mark the CFULL event time. The horizontal dotted lines in panels (**a**,**b**,**e**) mark the zero angle margin, the 10° command preference and the −20° elevator guard, respectively. The event marker belongs to this diagnostic integration, separately from the ordinary solver trial state. The elevator and acceleration insets use the same records and end at the event for CFULL. The input guard stops the model without simulating a saturated actuator response.

Command-acceleration and total-moment peaks increase in every common complete pair, while acceleration-moment changes have mixed signs. The lower elevator peaks therefore coexist with higher demands elsewhere in the realization chain. For S26/CVAT, RMSE over 0–2 s is nearly unchanged (0.690784 versus 0.690976 m), but over 2–45 s increases from 6.79949 to 11.3979 m. CF16 has attitude-lag RMS 1.42624°, and force-residual RMS rises from 17.3085 to 30.9531 N. This is not solely an initial transient. The 36/40 strong-

margin count combines configurations on five development cases and is not independent attainment of the 90% target. Section S17 reports refinements and bandwidth sensitivity. The comparison shows that changing command realization alters the observed outcomes and costs. Its scope is the implemented tracker and these reused cases.

Table 5. Dynamic-command comparison on five reused cases. Each entry has denominator eight configurations. Positive means complete with both sampled margins positive.

Case	DN Complete	DN Positive	CF16 Complete	CF16 Positive
S01	8	8	8	8
S26	4	2	8	8
S07	6	6	8	8
S08	8	8	8	8
S45	8	8	8	8

5.5. Sensitivity to Prescribed Estimation Errors

Table 6 retains every outcome of the 140 runs. Low and high error levels reduce completion and positive-margin counts substantially. At the high level, only three CV trajectories complete, all with a negative actual angle margin. A larger completion count is therefore not evidence of better protection. CFULL/CVAT have only 4/15 common complete low-error pairs, from two cases, and none at the high level. Comparisons restricted to survivors cannot support a robust ranking. Command-domain terminations concern the estimated-state command evaluation and are not automatically actual-state boundary crossings. The prescribed errors expose sensitivity without representing sensor, estimator or atmospheric validation.

Table 6. All prescribed-error outcomes. The 140 runs reuse five cases. Configurations and error streams are not independent case inputs.

Error	Runs	Complete	Request Stop	Domain Stop	Positive
Zero	20	19	1	0	18
Low	60	29	13	18	18
High	60	3	49	8	0

5.6. Independent-Input Numerical Evaluation in Two Sampling Ranges

The frozen generator accepted 50 of 51 candidates in H-I and 50 of 63 in H-X. Fourteen candidates failed nominal reference qualification before any controller outcome. All 400 planned integrations have records, with no unresolved technical outcomes or retries. Table 7 separates the two layers and retains all 50 cases per configuration. CAT and CVAT complete every case with positive sampled margins. CFULL completes 49/50 in H-I and 42/50 in H-X, with the remaining runs terminating at input-request guards. Its completed runs have positive sampled margins.

Table 7. Independent-input numerical evaluation, with denominator 50 per layer and configuration. Positive, strong and command criteria each require completion. Strong additionally requires only the prescribed angle-margin threshold.

Layer	Mode	Complete	Positive	Strong	Command
H-I	CV	50/50	47/50	37/50	48/50
H-I	CAT	50/50	50/50	39/50	44/50
H-I	CVAT	50/50	50/50	38/50	43/50
H-I	CFULL	49/50	49/50	38/50	44/50
H-X	CV	50/50	42/50	32/50	42/50
H-X	CAT	50/50	50/50	34/50	37/50
H-X	CVAT	50/50	50/50	33/50	36/50
H-X	CFULL	42/50	42/50	33/50	36/50

For each primary endpoint, the paired CFULL-minus-CVAT proportion difference is −0.02 in H-I (95% case-bootstrap interval $[-0.06, 0]$, exact and Holm-adjusted $p = 1$) and −0.16 in H-X (interval $[-0.26, -0.06]$, exact $p = 0.0078125$, Holm-adjusted $p = 0.03125$). Identical paired tables for the two endpoints are not two independent replications. Non-significance in H-I does not establish equivalence. A 50/50 proportion has Wilson interval $[0.9287, 1]$, which does not establish a population probability of one or the original 98% positive-margin target.

The strongest angle-margin counts are 39/50 (78%) in H-I and 34/50 (68%) in H-X, both below 90%. Continuous CFULL/CVAT contrasts cover only 49 and 42 common complete cases. Section S20 gives their paired intervals, including small changes that remain numerically qualified. No partial failed trajectory substitutes for a 45 s cost. The findings extend the evidence to new, qualification-conditioned inputs with frozen gains. They do not transfer the result to a different command architecture, sensing system or actuator model.

5.7. Isolated Speed Channel Recovery

The retained deterministic C0/CV comparison supplies a separate reason to keep the speed path available. Both start at 31.40 m/s above the study boundary and target 32.10 m/s. Speed-deficit exposure toward a 0.5 m/s interior margin decreases from 0.08256 to 0.04752 m (42.44%), and sustained sampled recovery shortens from 0.64 to 0.40 s. Peak force residual rises from 7.158 to 7.837 N and peak thrust from 36.49 to 49.83 N (Figure 5). This task-specific recovery benefit does not establish an unconditional benefit from adding V to CAT in the turning cases.

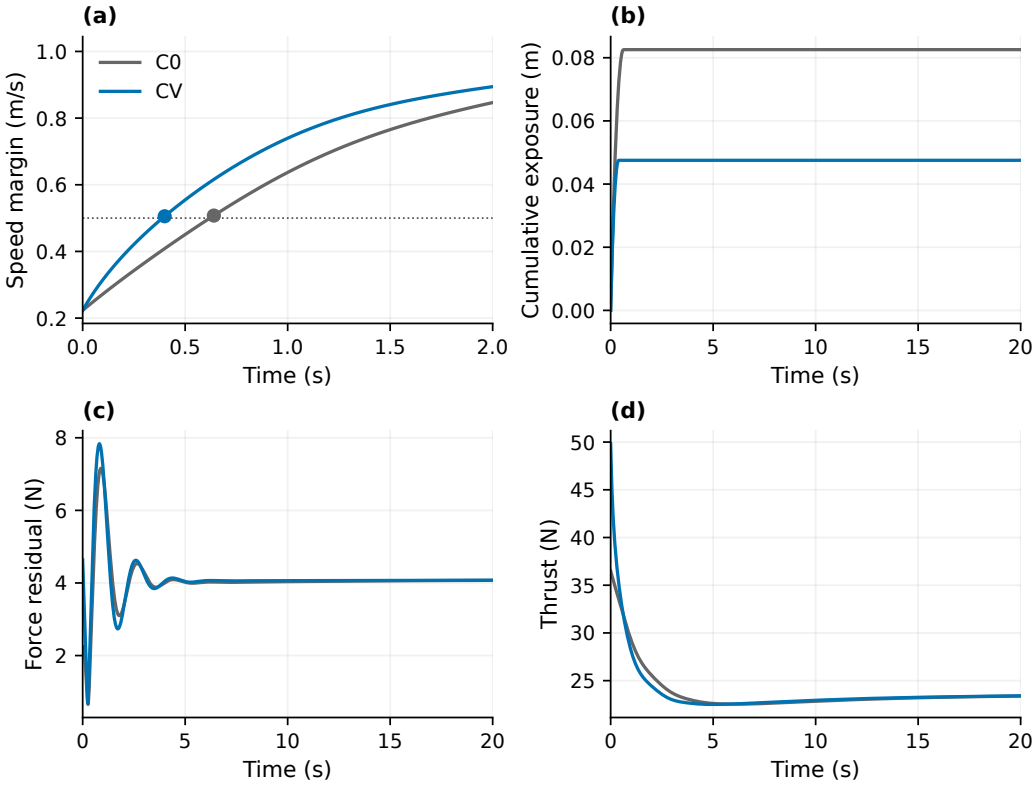


Figure 5. Deterministic isolation of the V force using C0 with no shaping and CV with only the V force, with $\kappa_V = 5$ J. In panel (**a**), the horizontal dotted line marks the speed-margin recovery threshold of 0.5 m/s. The markers indicate sustained recovery on the saved samples at 0.64 s for C0 and 0.40 s for CV. Panel (**b**) shows cumulative exposure over the full 20 s record in metres. Panels (**c**,**d**) show physical force residual norm and thrust request. Both cases begin above the study boundary. Reduced exposure is accompanied by increased peak force residual and thrust. Exposure is not an energy measure.

6. Discussion

6.1. What the Comparisons Support

The evidence supports configuration selection conditional on task and command realization. CAT uses fewer enabled paths and has lower position RMSE than CVAT in 47 of 48 matched turning/deceleration cases. Their margin differences have mixed directions, and the separate speed-recovery task supports retaining V as a task-dependent option. AF gives small recorded tracking-error reductions on common complete development trajectories, subject to numerical-resolution limits, alongside request terminations that depend on the other enabled paths. Independent inputs extend these observations under frozen D0 settings, particularly the CFULL/CVAT completion difference in H-X, while keeping the reused development set distinct.

The CF16 results materially qualify the original path-removal interpretation. A dynamic command realization removes the six DN terminations in the five-case comparison, at appreciable tracking and force-realization cost. The case for retaining AF therefore depends on the command realization and its associated costs. DN retains the large demand through a distinct calculation of the same command definition, indicating that the original finite difference increment explains only part of the observed difference. Same-definition numerical verification and a changed command architecture answer different questions.

The assessment procedure is to retain all outcomes, compare continuous metrics only on matched complete horizons, inspect controller maps at common states, and trace differences through command motion, moment and surface requests. The small direct force change in S26 illustrates why a path's instantaneous magnitude cannot by itself quantify its downstream effect. Common-state diagnostics remain local. Matching completion categories elsewhere do not establish the same mechanism at every state.

6.2. Actuator and External-Method Scope

The model applies admissible requests instantaneously and stops at an inadmissible request. A guard identifies demand outside this implementation's domain. An input-request termination does not establish loss of control in a physical aircraft. Post-saturation motion is not simulated. Real actuator bandwidth, delay, position/rate limits and constrained allocation introduce history dependence and moment residuals that can change both trajectories and configuration ordering. Their direction cannot be inferred from these simulations. CF16 changes command dynamics upstream and does not resolve this actuator limitation.

The implemented moment map is nonredundant and square. At a fixed regular state its exact inverse is unique. In the adopted model the pitch surface dependence is through the elevator. Bounded least-squares allocation can choose an admissible approximation [48], but exact redistribution of an out-of-bound request is not assured. The present controller also has no tracking-error integral state to which conventional integral anti-windup could simply be attached. A generalized compensation design would require an explicit state and mismatch interface, followed by a new closed-loop evaluation.

C0, DN and CF16 are internal comparisons, not external established-controller benchmarks. Attainable-moment pseudo-command limiting [35] and longitudinal high-order CBF protection with input magnitude/rate constraints [17] address related authority and feasibility questions with different control organizations. Adapting either requires matching the plant, reference, available information, controlled variables and constraints, while allowing appropriate method-specific tuning. The cited constrained-allocation algorithm is a lower-layer solver rather than a complete competing flight controller. Performance relative to these external controllers remains unevaluated.

6.3. Limits of Numerical and Theoretical Evidence

The original 48 cases and all local/filter/error studies reuse development inputs. The 100 new cases instead follow a frozen protocol, but remain conditional on nominal reference qualification, the stated sampling ranges and plant-informed initialization. The two layers must not be pooled into one population rate. The best strong-angle counts, 38/48 in development and 39/50 and 34/50 in the independent-input numerical evaluation, do not meet the original 90% target. Positive sampled margins also do not establish continuous-time invariance.

Numerical refinement supports classification repeatability only over the inspected settings and cases. Boundary requests and localized times remain sensitive. Invalid solver trials are not event roots. Several tiny paired differences change sign, and the historical bootstrap intervals do not include a complete numerical error budget. Neither near-unit ratios nor intervals excluding zero establish physical equivalence or practical superiority. Prescribed state-estimation errors markedly reduce completion, narrowing the useful interpretation of ideal-state results. No wind/turbulence model, sensor/estimator dynamics, actuator dynamics, hardware-in-the-loop or flight validation has been added.

The power identity retains moving centers, command motion and effective physical-input discrepancies, including terms without a fixed sign. Disabling AF does not remove its storage derivative. The separate ideal local matrix calculation is not the implemented physical closed-loop Jacobian. Likewise, constant-command properties of the filter subsystem do not prove stability of the moving-command augmented aircraft. The theoretical material identifies the coupling terms required by the architecture. Configuration judgments rely on the reported numerical comparisons.

7. Conclusions

This work develops a numerical architecture assessment for envelope feedback selection in fixed wing UAV tracking. Its contribution is to connect the state margin benefit of individual feedback paths to the tracking cost and downstream command and input demands required to realize them. Common state diagnostics separate direct changes in the control map from subsequent trajectory divergence, while conditional power accounting identifies the coupling and discrepancy terms retained after path removal. Together, these elements provide an engineering basis for assessing a shaping term through the complete realization chain rather than its immediate force or margin contribution alone.

The central finding is that feedback path selection and command generation are coupled design decisions. At the inspected conditions, a small angle of attack force produces substantial command acceleration and elevator demand, and an independent implementation of the same nominal derivative retains this response. A dynamic command tracker avoids the observed request terminations in the tested cases, but introduces greater tracking and force realization costs. These findings qualify a simple recommendation to remove the angle force. Its value depends on the surrounding feedback paths and command architecture, just as the benefit of speed feedback depends on the task.

For controller development, the assessment helps identify which paths merit retention and which realization stages require further attention before higher fidelity testing. Independent inputs extend the evidence beyond the development cases, although the stronger margin target remains unmet and estimation errors substantially reduce completion. The conclusions remain conditional on the sampling, numerical resolution and ideal actuation assumptions, without establishing continuous protection or superiority over external controllers. Their practical use is to guide subsequent evaluation with actuator dynamics, constrained allocation, realistic state estimation and atmospheric disturbances.

Supplementary Materials: The following supporting information can be downloaded at: https://www.mdpi.com/article/10.3390/app162110932/s1, Sections S1–S20 provide model coefficients, derivations, historical and final-gain comparisons, local and event diagnostics, dynamic command tracking, numerical and estimation-error studies, and independent-input protocols and statistics. Source-linked computational summary tables accompany the revision package.

Author Contributions: X.Z. contributed conceptualization and formal analysis. X.Z. and X.C. contributed methodology, investigation, and writing—review and editing. X.C. contributed software, data curation, writing—original draft preparation, and visualization. All authors have read and agreed to the published version of the manuscript.

Funding: This work was supported by the National Natural Science Foundation of China (grant No. 12402015) and the Natural Science Foundation of Inner Mongolia Autonomous Region of China (grant No. 2024QN01002).

Institutional Review Board Statement: Not applicable. The study consists of numerical simulation and does not involve human or animal participants.

Informed Consent Statement: Not applicable.

Data Availability Statement: The complete Supplementary Materials and accompanying computational data files provide the reported results and statistical summaries. The accompanying reproducibility package provides documented MATLAB R2018a code, frozen inputs, essential unrounded sampled outputs and Python scripts for reconstructing the principal tables and classifications. Version r2-1.0 is publicly available at https://github.com/xue794/uav-envelope-feedback-paths/tree/r2-1.0 (accessed on 4 Orctober 2026). Supplementary Section S13 defines the included data and verification scope.

Acknowledgments: The authors acknowledge the support of the Inner Mongolia Academician Workstation for New Energy Equipment and Operation Maintenance in IMUT. During the preparation of this manuscript, the authors used ChatGPT (GPT-6 Astra, OpenAI) for author-directed drafting based on author-provided scientific ideas, analysis, and results, as well as structural revision, language editing, and consistency checking. All AI-assisted content was reviewed and revised by the authors, who take full responsibility for the content of this publication.

Conflicts of Interest: Xiaolin Cao is employed by China Telecom Corporation Limited Heilongjiang Branch. The other author declares no conflicts of interest.

Abbreviations

The following abbreviations are used in this manuscript:

UAV	Unmanned aerial vehicle
GNA	Generic nonlinear aerodynamic
GTM	Generic Transport Model
AoA	Angle of attack
CBF	Control barrier function
RMSE	Root mean square error

References

1. Park, S.; Deyst, J.; How, J. A New Nonlinear Guidance Logic for Trajectory Tracking. In Proceedings of the AIAA Guidance, Navigation, and Control Conference and Exhibit, Providence, RI, USA, 16–19 August 2004; AIAA Paper 2004-4900. [CrossRef]
2. Beard, R.W.; Ferrin, J.; Humpherys, J. Fixed Wing UAV Path Following in Wind With Input Constraints. *IEEE Trans. Control Syst. Technol.* **2014**, *22*, 2103–2117. [CrossRef]
3. Trakas, P.S.; Bechlioulis, C.P. Robust Trajectory Tracking Control for Constrained Small Fixed-Wing Aerial Vehicles with Adaptive Prescribed Performance. *Appl. Sci.* **2023**, *13*, 7718. [CrossRef]
4. Enns, D.; Bugajski, D.; Hendrick, R.; Stein, G. Dynamic inversion: An evolving methodology for flight control design. *Int. J. Control* **1994**, *59*, 71–91. [CrossRef]

5. Sieberling, S.; Chu, Q.P.; Mulder, J.A. Robust Flight Control Using Incremental Nonlinear Dynamic Inversion and Angular Acceleration Prediction. *J. Guid. Control. Dyn.* **2010**, *33*, 1732–1742. [CrossRef]
6. Durham, W.C. Constrained control allocation. *J. Guid. Control. Dyn.* **1993**, *16*, 717–725. [CrossRef]
7. Johansen, T.A.; Fossen, T.I. Control allocation—A survey. *Automatica* **2013**, *49*, 1087–1103. [CrossRef]
8. Bakuła, K.; Ostrowski, W.; Pilarska, M.; Szender, M.; Kurczyński, Z. Evaluation and Calibration of Fixed-Wing Multisensor UAV Mobile Mapping System: Improved Results. *Int. Arch. Photogramm. Remote Sens. Spat. Inf. Sci.* **2019**, *XLII-2/W13*, 189–195. [CrossRef]
9. Garone, E.; Di Cairano, S.; Kolmanovsky, I. Reference and command governors for systems with constraints: A survey on theory and applications. *Automatica* **2017**, *75*, 306–328. [CrossRef]
10. Tee, K.P.; Ge, S.S.; Tay, E.H. Barrier Lyapunov Functions for the control of output-constrained nonlinear systems. *Automatica* **2009**, *45*, 918–927. [CrossRef]
11. Ames, A.D.; Xu, X.; Grizzle, J.W.; Tabuada, P. Control Barrier Function Based Quadratic Programs for Safety Critical Systems. *IEEE Trans. Autom. Control* **2017**, *62*, 3861–3876. [CrossRef]
12. Ames, A.D.; Coogan, S.; Egerstedt, M.; Notomista, G.; Sreenath, K.; Tabuada, P. Control Barrier Functions: Theory and Applications. In Proceedings of the 2019 18th European Control Conference (ECC), Naples, Italy, 25–28 June 2019; pp. 3420–3431. [CrossRef]
13. Xiao, W.; Belta, C. High-Order Control Barrier Functions. *IEEE Trans. Autom. Control* **2022**, *67*, 3655–3662. [CrossRef]
14. Xiao, W.; Belta, C.A.; Cassandras, C.G. Sufficient conditions for feasibility of optimal control problems using Control Barrier Functions. *Automatica* **2022**, *135*, 109960. [CrossRef]
15. Lombaerts, T.; Looye, G.; Ellerbroek, J.; Martin, M.R.Y. Design and Piloted Simulator Evaluation of Adaptive Safe Flight Envelope Protection Algorithm. *J. Guid. Control. Dyn.* **2017**, *40*, 1902–1924. [CrossRef]
16. Steffensen, R.; Gabrys, A.; Holzapfel, F. Flight Envelope Protections Using Phase Plane Limits and Backstepping Control. In Proceedings of the EuroGNC 2019, Milan, Italy, 3–5 April 2019.
17. Autenrieb, J. Quadratic Programming Approach to Flight Envelope Protection Using Control Barrier Functions. *J. Guid. Control. Dyn.* **2025**, *48*, 2622–2633. [CrossRef]
18. Tan, J.; Dong, Y.; Shao, P.; Qu, G. Anti-saturation adaptive fault-tolerant control with fixed-time prescribed performance for UAV under AOA asymmetric constraint. *Aerosp. Sci. Technol.* **2022**, *120*, 107264. [CrossRef]
19. Altunkaya, E.Ç.; Çatak, A.; Demir, M.; Koyuncu, E.; Özkol, I. Aircraft Stability and Safety: Practical Applications of Control Lyapunov and Barrier Functions. *J. Guid. Control. Dyn.* **2026**, *49*, 836–851. [CrossRef]
20. Atmaca, D.; Stroosma, O.; van Kampen, E.J. Design and Piloted Simulation of Envelope-Protected Control for Flying Wing Aircraft. *J. Guid. Control. Dyn.* **2026**, *49*, 1459–1474. [CrossRef]
21. Cao, S.; Yu, H. An Adaptive Control Framework for the Autonomous Aerobatic Maneuvers of Fixed-Wing Unmanned Aerial Vehicle. *Drones* **2022**, *6*, 316. [CrossRef]
22. Chen, W.; Guo, S.; Li, X.; Wang, S.; Wan, Z.; Jia, X.; Yao, Z. Robust Attitude Control of Fixed-Wing UAVs Under Near-Envelope Conditions Using a Hierarchical Adaptive NSGA-II. *Drones* **2026**, *10*, 532. [CrossRef]
23. Wang, J.; Li, J.; Liu, Y.; Wang, C.; Bu, C.; Feng, S.; Huo, M. Design and Wind Tunnel Test of Control Laws for High Angle of Attack Flight of Low-Aspect-Ratio Flying-Wing UAVs Based on NDI. *Drones* **2026**, *10*, 601. [CrossRef]
24. Willems, J.C. Dissipative dynamical systems part I: General theory. *Arch. Ration. Mech. Anal.* **1972**, *45*, 321–351. [CrossRef]
25. van der Schaft, A.; Jeltsema, D. Port-Hamiltonian Systems Theory: An Introductory Overview. *Found. Trends Syst. Control* **2014**, *1*, 173–378. [CrossRef]
26. Ortega, R.; van der Schaft, A.; Maschke, B.; Escobar, G. Interconnection and damping assignment passivity-based control of port-controlled Hamiltonian systems. *Automatica* **2002**, *38*, 585–596. [CrossRef]
27. Fujimoto, K.; Sakurama, K.; Sugie, T. Trajectory tracking control of port-controlled Hamiltonian systems via generalized canonical transformations. *Automatica* **2003**, *39*, 2059–2069. [CrossRef]
28. Fahmi, J.M.; Woolsey, C.A. Port-Hamiltonian Flight Control of a Fixed-Wing Aircraft. *IEEE Trans. Control Syst. Technol.* **2022**, *30*, 408–415. [CrossRef]
29. Fahmi, J.M.; Woolsey, C.A. Passivity Based Cross-Track Control of a Fixed-Wing Aircraft. In Proceedings of the EuroGNC 2022, Berlin, Germany, 3–5 May 2022; Paper CEAS-GNC-2022-023.
30. Willebeek-LeMair, I.; Widman, S.B.; Woolsey, C.A. Input-to-State Stable Energy-Based Position Tracking Control for Atmospheric Flight Vehicles. In Proceedings of the AIAA SCITECH 2025 Forum, Orlando, FL, USA, 6–10 January 2025; AIAA Paper 2025-2594. [CrossRef]
31. Panagou, D.; Stipanovic, D.M.; Voulgaris, P.G. Multi-objective control for multi-agent systems using Lyapunov-like barrier functions. In *Proceedings of the 52nd IEEE Conference on Decision and Control, Florence, Italy, 10–13 December 2013*; IEEE: Piscataway, NJ, USA, 2013; pp. 1478–1483. [CrossRef]
32. Alam, M.; Celikovsky, S. On the internal stability of non-linear dynamic inversion: Application to flight control. *IET Control Theory Appl.* **2017**, *11*, 1849–1861. [CrossRef]

33. Smeur, E.J.J.; Chu, Q.; de Croon, G.C.H.E. Adaptive Incremental Nonlinear Dynamic Inversion for Attitude Control of Micro Air Vehicles. *J. Guid. Control. Dyn.* **2016**, *39*, 450–461. [CrossRef]
34. Harkegard, O. Efficient active set algorithms for solving constrained least squares problems in aircraft control allocation. In Proceedings of the 41st IEEE Conference on Decision and Control, Las Vegas, NV, USA, 10–13 December 2002; Volume 2, pp. 1295–1300. [CrossRef]
35. Han, L.; Hu, J.; Wang, Y.; Cong, J.; Zhang, P. Design of Pseudo-Command Restricted Controller for Tailless Unmanned Aerial Vehicles Based on Attainable Moment Set. *Drones* **2024**, *8*, 101. [CrossRef]
36. Xia, Y.; Huo, M.; Zhao, X.; Wang, L.; Wang, J.; Yao, Y.; Pan, G.; Wang, C.; Yu, Z. Adaptive Nonlinear Dynamic Inversion with Ground Taxiing Dynamics for Trajectory Tracking and Safe Autonomous Take-Off/Landing of Fixed-Wing UAVs. *Drones* **2026**, *10*, 42. [CrossRef]
37. Stougie, J.; Pollack, T.; Van Kampen, E.J. Incremental Nonlinear Dynamic Inversion control with Flight Envelope Protection for the Flying-V. In Proceedings of the AIAA SCITECH 2024 Forum, Orlando, FL, USA, 8–12 January 2024; AIAA Paper 2024-2565. [CrossRef]
38. Hafner, S.; Autenrieb, J.; Steinert, A.; Holzapfel, F. Control Barrier Functions on a Pseudo Control Level for Safe Flight Control. In Proceedings of the EuroGNC 2026, Madrid, Spain, 5–7 May 2026; Paper CEAS-GNC-2026-010. [CrossRef]
39. Molnar, T.G.; Kannan, S.K.; Cunningham, J.; Dunlap, K.; Hobbs, K.L.; Ames, A.D. Collision Avoidance and Geofencing for Fixed-Wing Aircraft with Control Barrier Functions. *IEEE Trans. Control Syst. Technol.* **2025**, *33*, 1493–1508. [CrossRef]
40. Autenrieb, J.; Spiller, M.; Fisher, P.A.; Yoon, J.; Theodoulis, S.; Annaswamy, A. Closed-Loop Model-Based Control Barrier Functions with Application to Robust Flight Envelope Protection. *arXiv* **2026**, arXiv:2607.28830. Version 1, 30 July 2026.
41. Califano, F. Passivity-Preserving Safety-Critical Control Using Control Barrier Functions. *IEEE Control Syst. Lett.* **2023**, *7*, 1742–1747. [CrossRef]
42. Leung, C.H.; Paré, P.E. Port-Transversal Barriers: Graph-Theoretic Safety for Port-Hamiltonian Systems. *arXiv* **2026**, arXiv:2603.26578. Version 2, 12 September 2026.
43. Grauer, J.A.; Morelli, E.A. A Generic Nonlinear Aerodynamic Model for Aircraft. In Proceedings of the AIAA Atmospheric Flight Mechanics Conference, National Harbor, MD, USA, 13–17 January 2014; AIAA Paper 2014-0542. [CrossRef]
44. Lee, T.; Leok, M.; McClamroch, N.H. Geometric tracking control of a quadrotor UAV on SE(3). In *Proceedings of the 49th IEEE Conference on Decision and Control (CDC), Atlanta, GA, USA, 15–17 December 2010*; IEEE: Piscataway, NJ, USA, 2010; pp. 5420–5425. [CrossRef]
45. Swaroop, D.; Hedrick, J.; Yip, P.; Gerdes, J. Dynamic surface control for a class of nonlinear systems. *IEEE Trans. Autom. Control* **2000**, *45*, 1893–1899. [CrossRef]
46. Farrell, J.; Polycarpou, M.; Sharma, M.; Dong, W. Command Filtered Backstepping. *IEEE Trans. Autom. Control* **2009**, *54*, 1391–1395. [CrossRef]
47. Cordeiro, R.A.; Azinheira, J.R.; Moutinho, A. Cascaded Incremental Backstepping Controller for the Attitude Tracking of Fixed-Wing Aircraft. In Proceedings of the EuroGNC 2019, Milan, Italy, 3–5 April 2019.
48. Härkegård, O. *Efficient Active Set Algorithms for Solving Constrained Least Squares Problems in Aircraft Control Allocation*; Technical Report LiTH-ISY-R-2426; Linköpings Universitet, Department of Electrical Engineering: Linköping, Sweden, 2002; Technical Report Dated 6 May 2002.

Disclaimer/Publisher's Note: The statements, opinions and data contained in all publications are solely those of the individual author(s) and contributor(s) and not of MDPI and/or the editor(s). MDPI and/or the editor(s) disclaim responsibility for any injury to people or property resulting from any ideas, methods, instructions or products referred to in the content.